Extension of the prognostic model of sea surface temperature to rain-induced cool and fresh lenses

Hugo Bellenger, Kyla Drushka, William E. Asher, Gilles Reverdin, Masaki Katsumata, Michio Watanabe

To cite this version:

Hugo Bellenger, Kyla Drushka, William E. Asher, Gilles Reverdin, Masaki Katsumata, et al.. Extension of the prognostic model of sea surface temperature to rain-induced cool and fresh lenses. Journal of Geophysical Research. Oceans, 2017, 122 (1), pp.484 - 507. ⟨10.1002/2016JC012429⟩. ⟨hal-01491843⟩

HAL Id: hal-01491843
https://hal.science/hal-01491843v1

Submitted on 15 Oct 2021

AGU PUBLICATIONS

JGR

Journal of Geophysical Research: Oceans

RESEARCH ARTICLE

10.1002/2016JC012429

Key Points:

- A prognostic scheme to represent rain-induced cooling and freshening (near surface and skin layer)
- The simple scheme reproduces many aspects of the rain-induced surface lenses
- Preliminary results on the impact of the rain-induced lenses on climate and its variability

Correspondence to:
H. Bellenger,
hbellenger@jamstec.go.jp

Citation:
Bellenger, H, K Drushka, W Asher, G Reverdin, M Katsumata, and M Watanabe. (2017), Extension of the prognostic model of sea surface temperature to rain-induced cool and fresh lenses, *J. Geophys. Res. Oceans*, *122*, 484–507, doi:10.1002/2016JC012429.

Received 5 OCT 2016
Accepted 14 DEC 2016
Accepted article online 22 DEC 2016
Published online 25 JAN 2017
Corrected 15 MAY 2017 and
Corrected 13 AUG 2018

This article was corrected on 15 MAY 2017 and 13 AUG 2018. See the end of the full text for details.

Extension of the prognostic model of sea surface temperature to rain-induced cool and fresh lenses

Hugo Bellenger[1], Kyla Drushka[2], William Asher[2], Gilles Reverdin[3], Masaki Katsumata[1], and Michio Watanabe[1]

[1]JAMSTEC, Yokosuka-City, Kanagawa, Japan, [2]Applied Physics Laboratory, University of Washington, Seattle, Washington, USA, [3]LOCEAN, IPSL, Sorbonne Universités (UPMC, Univ. Paris 06)-CNRS-IRD-MNHN, Paris, France

Abstract The Zeng and Beljaars (2005) sea surface temperature prognostic scheme, developed to represent diurnal warming, is extended to represent rain-induced freshening and cooling. Effects of rain on salinity and temperature in the molecular skin layer (first few hundred micrometers) and the near-surface turbulent layer (first few meters) are separately parameterized by taking into account rain-induced fluxes of sensible heat and freshwater, surface stress, and mixing induced by droplets penetrating the water surface. Numerical results from this scheme are compared to observational data from two field studies of near-surface ocean stratifications caused by rain, to surface drifter observations and to previous computations with an idealized ocean mixed layer model, demonstrating that the scheme produces temperature variations consistent with in situ observations and model results. It reproduces the dependency of salinity on wind and rainfall rate and the lifetime of fresh lenses. In addition, the scheme reproduces the observed lag between temperature and salinity minimum at low wind speed and is sensitive to the peak rain rate for a given amount of rain. Finally, a first assessment of the impact of these fresh lenses on ocean surface variability is given for the near-equatorial western Pacific. In particular, the variability due to the mean rain-induced cooling is comparable to the variability due to the diurnal warming so that they both impact large-scale horizontal surface temperature gradients. The present parameterization can be used in a variety of models to study the impact of rain-induced fresh and cool lenses at different spatial and temporal scales.

1. Introduction

Gases, kinetic energy, heat (latent and sensible), and electromagnetic radiation are exchanged between the ocean and atmosphere through the air-sea interface. These fluxes both modulate and are modulated by the state of the ocean surface. For example, the net longwave infrared radiation flux, combined with the sensible and latent heat fluxes are responsible for the presence of a cool skin layer on the ocean surface [*Fairall et al.*, 1996; *Soloviev and Lukas*, 2006]. These cool skin layers of less than a millimeter depth are hypothesized to affect the air-sea exchange of trace gases [e.g., *Ward et al.*, 2004]. In addition to air-sea interaction, vertical and horizontal gradients in surface salinity and temperature, which are generated mostly through fluxes of heat and freshwater through the ocean skin layer, determine upper ocean stability, a critical factor in determining the dynamics of upper ocean circulation.

The ocean surface skin layer is also central to remote sensing of surface temperature and salinity. For instance, sea surface temperature (SST) provides important information about the heat content of the ocean mixed layer that is crucial for tropical variability modes such as El Niño. Similarly, sea surface salinity (SSS) contains integrated information on the air-sea freshwater flux [*Gordon and Giulivi*, 2008; *Gordon*, 2016], measurement of which is a main challenge to closing the global water cycle [*Schmitt*, 2008]. However, satellite mounted radiometers measure the temperature and salinity of the ocean surface skin layer, not temperature and salinity in the bulk ocean surface layer. Infrared and microwave radiometers used to measure temperature detect photons emitted from the uppermost millimeter of the ocean surface [*Donlon and Robinson*, 1997]. L-band radiometers, which are used to observe salinity by the satellite instruments SMOS, Aquarius, and SMAP, detect photons emitted from at most the upper few centimeters of the ocean [e.g., *Boutin et al*., 2016]. Therefore, satellite-based temperature and salinity retrievals are affected by ocean surface skin effects, with depths of a few tens of micrometers to a few thousands of micrometers.

It is known that under conditions with some combination of weak wind, high solar forcing, and precipitation, the upper few meters of the ocean can stratify with respect to temperature or salinity, and that these gradients can last for a few hours and up to a day [e.g., *Price et al*., 1996; *Reverdin et al*., 2012, 2013; *Asher et al*., 2014b]. Under these conditions, satellite measurements may not be representative of the actual state of the ocean mixed layer, which is typically monitored by moorings and Argo floats at depths of 1–10 m. Studies have, therefore, concentrated on evaluating the magnitude of the changes in surface temperature and salinity caused by diurnal warming [*Price et al*., 1986; *Fairall et al*., 1996; *Stuart-Menteth et al*., 2003; *Gentemann et al*., 2003] or rain-induced freshening [*McCulloch et al*., 2012; *Henocq et al*., 2010; *Boutin et al*., 2013, 2014; *Santos-Garcia et al*., 2014; *Drushka et al*., 2014, 2016] to distinguish the bulk mixed layer properties from satellite observations.

In addition to their importance for remote sensing, diurnal variations of SST, also called diurnal warm layers, can trigger atmospheric convection [*Sui et al*., 1997; *Bellenger et al*., 2010; *Ruppert and Johnson*, 2015, 2016] and, in addition, may play a role in modulating large-scale variability due to El Niño-Southern Oscillation or the Madden-Julian Oscillation [*Clayson and Weitlich*, 2007; *Bellenger and Duvel*, 2009; *DeMott et al*., 2015]. Because diurnal warm layers are ubiquitous in the tropical oceans, attention has mainly focused on understanding their behavior and effects on larger-scale processes. However, rainfall also affects near-surface thermal and haline stratification [e.g., *Reverdin et al*., 2012], and despite being the subject of a number of numerical, theoretical, and observational studies [*Katsaros and Buettner*, 1969; *Katsaros*, 1976; *Price*, 1979; *Miller*, 1976; *Schlussel et al*., 1997; *Craeye and Schlussel*, 1998; *Soloviev and Lukas*, 2006; *Reverdin et al*., 2012; *Asher et al*., 2014b; *Drushka et al*., 2014, 2016] less is known about the potential role of these freshwater lenses play in determining climate and climate variability.

Rainfall freshens the near-surface ocean and produces a stable stratification due to salinity that acts like a short-lived barrier layer, enabling to sustained cooler temperatures close to the surface [e.g., *Reverdin et al*., 2012]. Therefore, it is essential to take into account salinity stratification in order to describe and simulate rain-associated cooling. Note that this phenomenon is the opposite of the one described by *Asher et al*. [2014a] where positive salinity anomalies at the surface due to evaporation form in the presence of near-surface warming induced by the solar radiation. Due to inhomogeneous spatial and temporal distribution of precipitation, associated temperature variations could affect horizontal temperature gradients from scales as small as an individual rain event (order km to 10 s of km in the tropics) up to scales as large as the Inter-Tropical Convergence Zone, where it is well known that large-scale temperature gradients impact large-scale circulation and variability [e.g., *Chiang et al*., 2001]. In addition, *Li and Carbone* [2012] have recently shown that mesoscale SST gradients play a role in rainfall onset over the tropical ocean. Therefore, it is appropriate to conduct a detailed study on how both diurnal warming and precipitation drive horizontal SST gradients on a range of scales. To this end, a complete description of the effect of rain on variability in SST must include not only the surface cooling due to rain itself but the effect of the salinity stratification on the dynamics of the upper ocean.

The presence of vertical gradients in the upper ocean makes the terms SST and SSS rather ambiguous. Therefore, when precision is needed in the discussion, we adopt the terminology developed by the group for high resolution SST [*Donlon et al*., 2007] to distinguish the interface SST (T_{int}), the SST below the diffusive microlayer or cool skin ($T_{subskin}$) and the foundation temperature T_{fnd} that is the bulk temperature of the oceanic mixed layer. In addition, the temperature at a certain depth z (in meters) is noted T_z. This terminology and these notations are directly extended to SSS [*Boutin et al*., 2016].

Fresh lenses and diurnal warm layers are light wind phenomena and both are associated with stratification within the first meters of the ocean [e.g., *Fairall et al*., 1996; *Asher et al*., 2014a, 2014b; *Drushka et al*., 2016]. Therefore, we seek to represent both phenomena in a unified framework. Here, a simple prognostic scheme, developed initially to represent the continuous evolution of interface SST due to the cool skin effect and the formation of diurnal warm layers [*Zeng and Beljaars*, 2005; *Takaya et al*., 2010], is extended in order to take into account the effects of rain. Section 2 describes the two parts of the updated scheme: part 1, the diffusive microlayer at the air-sea interface, often referred to as the cool skin; and part 2, a near surface layer defined to be at most a few meters thick that corresponds to the thermohaline stratification associated with diurnal warm layers [*Price et al*., 1986; *Fairall et al*., 1996; *Zeng and Beljaars*, 2005; *Asher et al*., 2014a] and fresh lenses due to precipitation [*Reverdin et al*., 2012; *Asher et al*., 2014b; *Drushka et al*., 2016]. Section 3 provides validation and statistics, and explores the sensitivity of the numerical scheme to environmental forcing. Section 4 discusses preliminary results on the potential impact of freshwater lenses on the tropical climate. Section 5 provides a summary and discussion of the results.

2. The Prognostic Scheme

2.1. The Diffusive Microlayer

The diffusive microlayer at the sea surface is the thin layer no more than a few millimeters thick where viscous stresses damp turbulence motions. Within the microlayer, the vertical transfers of heat, salt, and gases are due primarily to molecular diffusion [see *Soloviev and Lukas*, 2006 for a comprehensive description of the microlayer]. The microlayer is of particular importance as it controls exchanges of heat and chemical species between the ocean and atmosphere and because it affects temperature and salinity retrieved by remote sensing techniques.

The diffusive microlayer for heat is also called the thermal sublayer, and within this layer water temperature decreases toward the surface due to the cool skin effect caused by the ocean losing heat through a net upward surface flux [*Saunders*, 1967]. In the absence of rain, evaporation at the ocean surface is also responsible for an increase in salinity with decreasing depth in the diffusive sublayer, although the depths of the thermal sublayer and the diffusion sublayer for salt are in general not the same due to the large difference in diffusivity between heat and salt. In the presence of rain, salinity in the diffusive sublayer decreases toward the surface due to the freshwater input at the surface [*Schlussel et al*., 1997]. In the absence of other effects, the freshening due to rain would decrease surface density and lead to a stable density stratification in the microlayer. However, in general raindrops are colder than the sea surface and this cooling due to rain increases surface density. Therefore, the net effect of rain on stratification in the microlayer is determined by the interplay of the stabilizing effect of the freshening and the destabilizing effect of cooling. In addition, rain induces additional surface stress and turbulent mixing due to the kinetic energy of rain droplets.

The governing equations describing temperature and salinity in the microlayer in the scheme presented here are based on the work of *Saunders* [1967], but incorporate the work of *Fairall et al*. [1996] for the microlayer thermal structure and the work of *Schlussel et al*. [1997], *Craeye and Schlussel* [1998], and *Soloviev and Lukas* [2006] for the microlayer haline structure, including the effects of rain in increasing the surface stress [*Caldwell and Elliott*, 1971] and in inducing turbulence and damping gravity waves [*Tsimplis and Thorpe*, 1989]. Note that swell is also known to have an effect on the microlayer thermal structure [*Jessup and Hesany*, 1996; *Wick and Jessup*, 1998]. Yet, this effect depends on the relative direction between the wind stress and swell waves [*Jessup and Hesany*, 1996]. Its inclusion would require the use of a wave model, which is not done here. Finally, the effect of rain on surface films is not considered as it has been shown to be negligible [*Schlussel et al*., 1997].

Saunders [1967] assumed that the vertical gradients of temperature (T) and salinity (S) in the molecular layer were linear, and that the difference between the bulk and skin values in each are given by:

$$\begin{aligned}\Delta T &= \frac{\delta_T}{\rho_w c_w D_H}\left(Q_\mu + I_s f_s(\delta_T)\right)\\ \frac{\Delta S}{S} &= \frac{\delta_S}{D_S}\left(E - R_\mu\right)\end{aligned} \tag{1}$$

where ΔT and ΔS are the differences $T_{int} - T_{subskin}$ and $S_{int} - S_{subskin}$, respectively; δ_T and δ_S are the depths of the thermal and haline molecular diffusion layers, respectively; ρ_w is the density of water, c_w is the specific heat capacity of water, D_H is the molecular diffusivity of heat in water, D_S is the molecular diffusivity of salt in water, Q_μ is the microlayer net heat flux, I_S is the surface solar radiation flux, $f_S(\delta_T)$ is the fraction of shortwave solar radiation absorbed in the microlayer, and the evaporation (E) and the fraction of the rain deposited in the microlayer (R_μ) are in meters per second. Fluxes are defined as positive downward. Typically, δ_T is on the order of 500 μm and δ_S is on the order of 50 μm.

Because the kinematic viscosity of water (i.e., diffusivity of momentum) is approximately the same as the diffusivity of heat, *Saunders* [1967] assumed that the thermal diffusion layer depth was proportional to the viscous layer depth. Using this assumption, *Saunders* [1967] rewrote (1a) by taking δ_T to be equal to a proportionality constant λ (the so-called Saunders constant) multiplied by the kinematic viscosity, ν (m^2 s^{-1}), divided by the water-side friction velocity, u_{*w} *that is,* $\delta_T = \lambda\nu/u_{*w}$ valid for shear induced turbulence. *Saunders* [1967] *then assumed that* δ_S *could be estimated from* δ_T *using classic boundary layer theory, which predicts that the relative thicknesses of the diffusive boundary layers for heat and mass scales as the two-thirds power of the ratio of their molecular diffusivities. Based on these considerations (1) is rearranged as*

$$\Delta T=\frac{\lambda\nu}{\rho_w c_w D_H u_{*w}}\left(Q_\mu+I_s f_s(\delta_T)\right)$$
$$\frac{\Delta S}{S}=\lambda\left(\frac{D_H}{D_S}\right)^{2/3}\frac{\nu c_w}{\rho_w c_w D_H u_{*w}}\left(\frac{Q_{Lat}}{L_v}-P_\mu\right) \tag{2}$$

where precipitation rate P_μ is defined as a mass flux per unit area with units of kg m^{-2} s^{-1}, Q_{Lat} is the latent heat flux, L_V is the latent heat of vaporization. Following Zeng and *Beljaars* [2005], λ and $f_S(\delta_T)$ are determined using expressions proposed by *Fairall et al*. [1996]. Although *Saunders* [1967] assumed λ to be constant, the expression for λ given by *Fairall et al*. [1996] (their equation (14)) models λ to depend on whether turbulence is generated by shear or convection.

The net flux, Q_μ, includes not only the bulk air-sea fluxes of latent and sensible heat and the net longwave radiative flux, but also the sensible heat flux due to rain, Q_{Rain} [*Gosnell et al*., 1995]:

$$Q_\mu=Q_{Lat}+Q_{Sens}+I_L+Q_{Rain}(1-f_V(\delta_S)) \tag{3}$$

where Q_{Sens} is the sensible heat flux, I_L the net longwave radiative flux, and f_V is the decay function of the freshwater volume due to rain such that $f_V(\delta_S)$ is thus the fraction of the total rain volume that penetrates at least up to depth δ_S. Note that the net flux that appears in the expression for λ given by *Fairall et al*. [1996] includes the buoyancy effects of salinity due to evaporation and rain. It reads:

$$Q_{b\mu}=Q_{Lat}+Q_{Sens}+I_L+Q_{Rain}(1-f_V(\delta_S))+\frac{\beta c_w}{\alpha}S\left(\frac{Q_{Lat}}{L_v}-P_\mu\right) \tag{4}$$

The fresh water flux into the surface microlayer is defined by

$$P_\mu=P.(1-f_V(\delta_S)) \tag{5}$$

where $\alpha=-\rho^{-1}(\partial\rho/\partial T)$ and $\beta=\rho^{-1}(\partial\rho/\partial S)$ are the thermal expansion and haline contraction coefficients.

The mixing in the microlayer that is due to the kinetic energy input by the penetrating raindrops is parameterized as an equivalent stress τ_k [*Schlussel et al*., 1997; *Craeye and Schlussel*, 1998; *Soloviev and Lukas*, 2006]. This, along with the rain-induced surface stress τ_{rain} [*Caldwell and Elliott*, 1971], is added to the surface stress due to the wind. Therefore, the friction velocity in the presence of rain is written as:

$$u_{*w}=\left[\frac{1}{\rho_w}\left(\tau_{wind}+(1-f_V(\delta))\tau_{rain}+(f_V(0)-f_V(\delta))\tau_k\right)\right]^{1/2} \tag{6}$$

with $\delta=\delta_T$ or δ_S depending on whether this friction velocity is applied to the thermal or salt diffusion layer in (2). Note that $f_V(0)$ is the fraction of rain penetrating the ocean and is not equal to 1 as only the largest raindrops penetrate [see f_0 below and *Schlussel et al*., 1997]. The additional stresses are:

$$\tau_{rain}=0.85U_{10}R \tag{7}$$

where R is the rain rate and U_{10} is the 10 m wind, and

$$\tau_k=\rho_w(F_k/\rho_w)^{2/3} \tag{8}$$

where F_k, the flux of kinetic energy carried by rain, is computed following *Craeye and Schlussel* [1998, see also *Soloviev and Lukas*, 2006], assuming a Marshall-Palmer raindrop size distribution [*Marshall and Palmer*, 1948] and the empirical relation for the terminal velocity of raindrops proposed by *Best* [1950]. F_k is then approximated by a simple power function of R fitted to the exact solution provided by *Craeye and Schlussel*

[1998] and *Soloviev and Lukas* [2006]: $F_k(R)=aR^b$, where R is given in millimeters per hour and $a=4\times10^{-4}$, and $b=1.3$.

Finally, for δ close to zero, $f_V(\delta)$ is approximated by:

$$f_V(\delta)=\delta\sum\zeta_l\ \exp(-\psi_l\Lambda\delta/a)+f_0 \tag{9}$$

where a is the coefficient of proportionality between raindrop radius and penetration depth and has the numerical value of 100 [*Manton*, 1973]. The coefficients ζ_l and ψ_l are provided by *Schlussel et al.* [1997] (see their Table 1), and f_0 the fraction of raindrops penetrating water surface:

$$f_0=(1+2\Lambda r_c+4\Lambda^2 {r_c}^2+8\Lambda^3 {r_c}^3)\ \exp(-2\Lambda r_c) \tag{10}$$

where r_c is the critical radius of droplets below which their kinetic energy is too small to overcome surface tension and penetrate the ocean and it is assumed that $r_c=4\times10^{-4}$ m [*Oguz and Prosperetti*, 1991]. The coefficient Λ is defined in terms of R as $\Lambda=4.1R^{-0.21}$ [*Marshall and Palmer*, 1948].

The Marshall-Palmer drop size distribution is given by where $n(r)$ is the number of drops per unit volume of air and unit increment of radius and n_0 is a constant. There is some discussion in the literature concerning the appropriate value for n_0. For example, *Craeye and Schlussel* [1998] chose a value of n_0 that is twice as large as used by *Marshall and Palmer* [1948] and *Soloviev and Lukas* [2006]. Furthermore, *Craeye and Schlussel* [1998] also use a different relationship for estimating the droplet terminal velocity, which is used to estimate (8), than the one used by *Soloviev and Lukas* [2006]. These two differences lead to τ_k being almost twice as large in *Craeye and Schlussel* [1998] than in *Soloviev and Lukas* [2006] for the same rain rate R. Here we use the set of parameters used by *Soloviev and Lukas* [2006].

2.2. Near-Surface Stratification

Below the diffusive microlayer, advection and turbulent mixing controls the vertical flux of heat and salt. Here, in order to model the time evolution of T and S beneath the diffusive microlayer ($T_{subskin}-T_{fnd}$ and $S_{subskin}-S_{fnd}$), the *Zeng and Beljaars* [2005] prognostic scheme for diurnal warm layers is extended to the one-dimensional salinity budget. Following *Zeng and Beljaars* [2005], the profiles of S and T with respect to depth are assumed to have the following idealized form:

$$X(z)=X_{-\delta}-[(z+\delta)/(-d+\delta)]^{\eta}(X_{-\delta}-X_{-d}) \tag{11}$$

Where $-d<z<-\delta$, $X=T$ or S, and $-d$ is the base of the warm layer or the freshwater lens and is assumed to be constant and equal to -3 m as in *Zeng and Beljaars* [2005]. In other words, we assume that $T_{fnd}=T_{-d}$ and $S_{fnd}=S_{-d}$. *Zeng and Beljaars* [2005] assume that, in the case of diurnal warming, η is constant with a value of 0.3.

Although (11) is the same for S and T, there can be differences between the profiles corresponding to diurnal warm layers and rain-induced lenses. In the case of diurnal warm layers, the stratification is induced by the downwelling solar shortwave radiation that penetrates several meters deep into the ocean (e.g., more than 40% of shortwave radiation reaches 5 m depth). On the other hand, in the case of a rain-induced fresh lens, the stratification results from the freshwater flux due to rain that penetrates to a depth of at most a few tens of centimeters [*Schlussel et al*., 1997; *Soloviev and Lukas*, 2006]. This difference means that the input of freshwater that drives T and S gradients is at the surface, whereas the input of heat that drives the diurnal warm layer is more distributed through the water column. Therefore, it might be expected that the vertical profiles for T and S in the fresh lens are more tightly linked to the surface wind forcing than in the case of diurnal warming. A small η in (11) corresponds to strong gradient of X close to the surface whereas when it is large and close to 1, the gradient is less steep. Under conditions where a fresh lens forms (i.e., the condition $(S_{-\delta}-S_{-\mathrm{d}})<0$ is met), the effects of wind speed are, therefore, included by using a wind speed-dependent value of η in (11) for both T and S: for $U<2$ m s^{-1} then $\eta=0.133$, for 2 m s$^{-1}\leq U<15$ m s^{-1} then $\eta=U/15$, and $\eta=1$ for $U\geq15$ m s^{-1}. This constraint on η for weak winds is imposed to avoid possible numerical problems for $U=0$ m s^{-1}, and because in very weak wind conditions the turbulence induced by penetrating raindrops should mix the upper few tens of centimeters of the ocean, limiting the steepness of the salinity gradient in the diffusive microlayer. Outside of fresh lenses (for $(S_{-\delta}-S_{-\mathrm{d}})\geq0$), the original constant value of $\eta=0.3$ is used.

There are insufficient field observations of fresh lenses to develop robust statistics on the wind dependency of their vertical structure, particularly for weak winds. Therefore, it is expected that expressions for η will be refined as more observations become available. The choice of this formula for η will be justified a posteriori by analysis of the statistics of rain-induced freshening and cooling that are computed in an idealized framework. These results are presented in Section 3.2. Finally, it would be more realistic to have η depend on wind speed for warm layers as well as fresh lenses. However, consideration of this is out of the scope of the present study.

The turbulent diffusion coefficient that characterizes the vertical movement of salinity and temperature is parameterized following *Large et al*. [1994] as

$$K_w(z)=ku_{*w}(-z)/\phi_t(-z/L) \tag{12}$$

Where $k = 0.4$ is the Von Karman constant and the stability function ϕ_t (nondimensional temperature gradient from the Monin-Obukhov similarity theory) is taken from the refined version of the scheme proposed by *Takaya et al*. [2010]. The Monin-Obukhov length is $L = u_{*w}^3/(kB)$ where B is the buoyancy flux, defined as

$$B=\frac{\alpha g}{\rho_w c_w}\left(Q_{Lat}+Q_{Sens}+I_L+Q_{Rain}+I_S f_S(-d)\right)-\frac{\beta g S}{\rho_w}\left(Q_{Lat}/L_v-P\right) \tag{13}$$

where g is the acceleration of gravity. Note that B is proportional to the sum of the net flux including buoyancy effects of rain as defined in (4) and of the fraction of solar radiation absorbed in the freshwater lens or the warm layer. Then, following *Zeng and Beljaars* [2005], the one-dimensional heat and salinity budgets can be vertically integrated from $-$d to $-\delta$ using (11) to give a prognostic equation for $T_{subskin}$ and $S_{subskin}$ evolution:

$$\begin{aligned}\partial(T_{-\delta}-T_{-d})/\partial t&=\frac{Q_{Lat}+Q_{Sens}+I_L+Q_{Rain}+I_S f_S(-d)}{d\rho_w c_w \eta/(\eta+1)}-\frac{(\eta+1)ku_{*w}}{d\phi_t(d/L)}(T_{-\delta}-T_{-d})\\ \partial(S_{-\delta}-S_{-d})/\partial t&=S_{-\delta}\frac{Q_{Lat}/L_v-P_\mu}{d\rho_w \eta/(\eta+1)}-\frac{(\eta+1)ku_{*w}}{d\phi_t(d/L)}(S_{-\delta}-S_{-d})\end{aligned} \tag{14}$$

As discussed by *Zeng and Beljaars* [2005], equation (14) with L computed using equation (13) is only applicable to cases where (i) the overall stratification is unstable ($\rho_{-\delta} - \rho_{-d} > 0$) and (ii) the overall stratification is stable ($\rho_{-\delta} - \rho_{-d} < 0$) with a positive buoyancy flux ($B > 0$). In these cases, we use the expression of ϕ_t proposed by *Takaya et al*. [2010]. When the buoyancy flux given by (13) is negative for the case of stable stratification ($\rho_{-\delta} - \rho_{-d} < 0$ and $B < 0$), the system is not in the equilibrium required for the application of the similarity theory. In this latter case, *Zeng and Beljaars* [2005] then derive an alternative expression for the buoyancy flux to be used in the computation of L. Following them, we assume that $\phi_t(d/L)=5d/L$ and that the density in the lens can be considered as constant in time. Using the definition of the thermal expansion and haline contraction coefficient this can be written as n(r). This expression is used to combine the two parts of (14). By rearranging the terms of the combined equation, we get the alternative expression to (13) for B:

$$B=\left(\frac{-\eta g(\rho_{-\delta}-\rho_{-d})}{5d\rho_w}\right)^{1/2}u^2{}_{*w} \tag{15}$$

This alternative expression is then used to compute an alternative L that is used in the integration of (14) to compute the evolution of T and S.

As mentioned previously, the total friction velocity in the presence of rain is given by the linear sum of the wind stress, the rain stress, and the kinetic energy imparted to the water surface by the downward motion of the raindrops (see (6)). However, in order to simplify the calculations, it is assumed that the equivalent stress, τ_k (see (8)), due to mixing induced by penetrating droplets is negligible compared to τ_{wind} and τ_{rain} below the microlayer. This assumption is justified because in contrast to τ_{wind} and τ_{rain} (see (7)), which are tangential stresses on the ocean surface, τ_k represents mainly the deposition of vertically directed kinetic energy at the surface. These vertical motions caused by penetrating raindrops enhance the mixing of seawater down to the rain penetration depth and, therefore, impact salinity and temperature profiles in the upper tens of centimeters. This turbulence is very important for the microlayer evolution [*Schlussel et al*., 1997] but its effect should decay rapidly away from the interface. Indeed, in the scheme used here, $f_v(z)$

decreases rapidly as depth increases: following *Schlussel et al.* [1997], $f_v(z = 1\ \text{m})$ is less than 0.5% for $R = 100\ \text{mm h}^{-1}$. Therefore, penetrating raindrops should not affect T and S profiles at the base of the lens that is on the order of 1 to few meters [*Drushka et al.*, 2016]. Note in addition that τ_{rain} can here be considered as a pure surface forcing regardless of the depth of the fresh lens so that the factor with $f_v(\delta)$ in (6) vanishes. Using these simplifications, u_{*w} is given in terms of the linear sum of τ_{wind} and τ_{rain} as in *Caldwell and Elliott* [1971]

$$u_{*w} = \left[\frac{1}{\rho_w}\left(\tau_{wind} + \tau_{rain}\right)\right]^{1/2} \tag{16}$$

where τ_{rain} is defined by (7). This simplified expression (16) for the friction velocity is only used in (14) and (15) corresponding to changes in T and S below the microlayer. Although the effect of the vertical kinetic energy is neglected here, its contribution to the total shear stress could be included in models with high vertical resolution within the ocean top meter such as the Generalized Ocean Turbulence Model (GOTM) [*Burchard et al.*, 1999]. Alternatively, its effect could be included in this model by making T and S idealized profiles, given by (11), dependent on the rain rate.

Finally, because the spatial scales for freshwater lenses generated by tropical rainstorms are in general smaller than the spatial scales of diurnal warm layers, the effect of horizontal spreading under the action of horizontal buoyancy gradients should not be neglected, especially at low wind speed. The effect of this lateral spreading on the temperature and salinity budget in the lens can be taken into account by a vertical advection term , with $X = T$ or S and w the vertical velocity of the lens bottom. The vertical velocity is assumed to be positive (and upward) during the spreading based on considering a simplified "box-model" for the fresh lens evolution [*Fay*, 1969; *Huppert and Simpson*, 1980]. In this model, the lens is a cylinder of radius l and depth h that spreads with a constant volume $V = \pi h l^2$. Since V is constant, as l increases, h must decrease and, therefore, the base of the lens moves upward.

When rain deposits freshwater on the ocean surface, this sets up a density gradient between the fresh lens and the surrounding seawater. Because the density gradient is large, the viscous forces are small compared to the gravitational and inertial forces, and the lens then spreads as a gravity current with the inertial and gravitational forces in balance [*Fay*, 1969]. Since the inertial force is defined by $\rho l/t^2$ and the gravitational force is given as $g(\rho - \rho')h/l$, equating the two forces and using the constant volume constraint results in the radius of the lens evolving as $l - l_0 = (g'V/\pi)^{1/4} t^{1/2}$ where $g' = g(\rho - \rho')/\rho$ is the reduced gravity. The constant volume assumption is valid if diffusion and mixing across the edge and base of the lens are neglected. Therefore, the time-dependent depth of the lens can be written as $h = h_0/[\pi(1 + (t/t_0)^{1/2})^2]$ where $t_0 = l_0/(g'h_0)^{1/2}$ is the timescale of the lens spreading, and h_0 and l_0 are the initial depth and radius of the lens, respectively. Assuming the time rate of decrease of the depth of the lens, w, is given by h_0/t_0, then the advective term for the change in T or S in the presence of a fresh water lens (where <0) is given by

$$-w\partial X/\partial z \approx -\frac{(\eta+1)}{d}\frac{{h_0}^{3/2}}{l_0}\left(g\frac{|\rho(T_{-\delta}, S_{-\delta}) - \rho(T_{-d}, S_{-d})|}{\rho_w}\right)^{1/2}(X_{-\delta} - X_{-d}) \tag{17}$$

where $X = T$ or S and $h_0 = d$ and is defined to be equal to 3 m. The effect of the lateral spreading of the fresh lens on the evolution of T and S can now be included by adding (17) onto (14). As written (17) does not take into account the end-stage behavior of the lens. As time increases, the Froude number increases and the viscous force overcomes the inertial force to counteract gravity, resulting in a reduced spreading rate.

Note also that including the effect of lateral spreading has no impact on the maximum salinity decrease that takes place during a rain event. Lateral spreading acts to decrease the lifetime of the fresh lens and, therefore, limit the decrease in temperature of the lens in light wind conditions. Indeed, as discussed by *Reverdin et al.* [2012] and shown below, the temperature of the lens decreases due to the heat loss caused by the net upward heat flux after the rain has ceased. Because there is little vertical mixing across the base of the lens at low wind speeds, this heat loss comes mainly from the stable fresh lens. A decrease in the lifetime of the lens implies there is less time for the heat flux to decrease temperature.

The relaxation term (17) decreases as l_0 increases, making it an important parameter in modeling the evolution of a fresh lens. However, estimating l_0 from the forcing functions such as R is not straightforward although some empirical evidence suggests such a dependency exists [e.g., *Hamada et al*., 2014]. Because a reliable method for predicting r_0 is unavailable at present, it must be estimated by other means. In the absence of better solution, l_0 can be defined in terms of the horizontal resolution of the model as $l_0 = (\varphi \Delta_x \Delta_y / \pi)^{1/2}$, where Δ_x and Δ_y are the horizontal grid spacing of the model and φ is the area fraction covered by precipitation, which can be set to 1 for stratiform rain or in the range of 0.1–0.3 for convective rain. Alternatively, if field data are available it can be estimated from the horizontal extent of the convective echoes from rain radar observations.

In situ observations of the spreading of a rain-produced freshwater lens are limited, complicating the testing of the model described here. A numerical study performed by *Soloviev and Lukas* [2006] suggests that a fresh lens spreads with a timescale on the order of several hours for a lens with $l_0 = 2$ km. In contrast, *Soloviev et al*. [2015] performed a three-dimensional large eddy simulation for a lens having $h_0 = 5$ m, $l_0 = 20$ m, and characterized by a density difference across the base of the lens of 0.45 kg m^{-3}. They found that the lens lost more than 50% of its depth within the first 500 s. If the same density difference, h_0, and l_0 are used in the simple model presented here, it is found that $t_0 = 130$ s, which suggests that it may overestimate the speed of the relaxation and, Therefore, underestimate both the lens lifetime and temperature decrease. However, note that even for a density difference as large as 2 kg m^{-3}, t_0 is greater than 2 days for $l_0 = 50$ km, which shows that a large fresh lens spreads slowly. This might imply that lateral spreading of fresh lenses is a minor factor in their evolution. However, although not shown here the role of fresh lens spreading may be nevertheless important when using relatively low temporal resolution forcing parameters.

Finally, note that a number of processes are not taken into account explicitly in the present scheme. The effect of Langmuir turbulence, which is parameterized in the refined scheme presented by *Takaya et al*. [2010], is not included since it requires a wave model. However, Langmuir turbulence is expected to be important only at relatively high wind speeds when rain-induced cooling and freshening are weak.

Oceanic internal waves can affect surface T and S by modulating the entrainment at the strongly stratified base of warm layers [e.g., *Farrar et al*., 2007] and, by inference, also at the base of rain-induced fresh lenses. However, uncertainties on the source of these waves and their characteristics make it difficult to include their effects in the present scheme.

Finally, near-surface stratification, due to the diurnal warming or freshwater flux, traps the surface wind stress close to the surface. This creates a wind-driven current in the uppermost meters of the ocean also known as a “slippery sea” [*Houghton*, 1969; *Woods and Strass*, 1986; *Kudryavtsev and Soloviev*, 1990; *Sutherland et al*., 2016] for which Coriolis force may be important even at sub-inertial timescales [*Price et al*., 1986; *Noh et al*., 2010]. There is growing evidence that these shallow jets may lead to shear instabilities [*Sutherland et al*., 2016] that generate mixing at the base of the diurnal warm layer. Further research on their existence and characteristics are needed in the case of rain-induced lenses.

2.3. Scheme Implementation

In summary, the scheme computes the evolution of (i) the difference between T and S below the microlayer (sub-skin) and T_{fnd} and S_{fnd} with (14) and (ii) the difference of T and S across the microlayer with (2) given the air-sea fluxes: sensible and latent heat, solar and infrared radiation, surface wind stress, and rain rate. Equation (14), with the addition of (17) to its right-hand side, is integrated in time (with a 1-min time step) to give the evolution of $T_{subskin}$ and $S_{subskin}$ knowing the evolution of T_{fnd} and S_{fnd}. The initial values of the subskin T and S are set to be T_{fnd} and S_{fnd}, respectively. When a stable stratification is present, the expression for the buoyancy flux in (14) changes from (13) to (15) if (13) gives a negative result. Then, the difference of T and S across the microlayer is calculated using (2) to give T_{int} and S_{int}. The friction velocity is computed using (6) for the computation of the cross-microlayer differences in T and S, but using the simplified expression (16) for the computation of the subskin-foundation differences.

We use COARE3 algorithm [*Fairall et al*., 2003] to compute the air-sea sensible and latent heat fluxes from T_{int}, surface air temperature, pressure, wind speed, and relative humidity (RH). Downward shortwave and longwave radiation fluxes are computed as in GOTM [*Burchard et al*., 1999] based on the formulas of *Reed* [1977] and *Clark et al*. [1974], respectively. The shortwave radiation is computed for a given location, date, and time as a function of cloud cover fraction. The net longwave radiation is estimated from RH, air temperature, T_{int}, and cloud cover fraction.

This scheme is first compared to observational data of fresh and cool lenses. In situ measurements are then used to compute the fluxes and the time evolution of T and S. Idealized simulations with fixed values of wind, cloud cover, air temperature, pressure, and humidity, and a Gaussian (in time) rain event are also performed to derived statistics on the fresh lenses produced by the scheme and to study their sensitivity to the imposed wind speed, the maximal rainfall rate, the duration of the rain event, and the time of the day when it occurs. Finally, following *Drushka et al*. [2016] we use 6-hourly surface parameters from ERA-Interim [*Dee et al*., 2011] and 3-hourly CMORPH precipitation [*Joyce et al*., 2004] in order to illustrate the potential impact of the scheme on ocean surface variability on a larger scale. In this case, the forcing parameters are linearly interpolated to match the 1-min time step of the scheme.

3. Validation of the Scheme

3.1. Tests Using Observational Data

During the Palau2013 cruise in June 2013 near Palau Island in the tropical western Pacific Ocean, R/V Mirai deployed a thermistor chain (T-Chain) with a sensor every ~0.7 m between depths of 0 m and 12 m in order to measure temperature profiles within the first meters of the ocean. Using the vertical motion of the boat caused by surface waves, it is possible to derive profiles of temperature with a vertical resolution of 0.2 m. In addition, a Sea Snake [*Fairall et al*., 1997] was used, consisting of two thermal sensors mounted on a towed flexible tube that lies on the ocean surface when towed above speeds of 2.5 m s^{-1} [e.g., *Kawai et al*., 2006]. One of the sensors, designated T_{0m} (SS0.05m), is mounted 0.05 m from where the tube attaches to the tow line and measures seawater temperature at a depth of a few centimeters. The second sensor, designated T_{0m} (SS1m), is attached to the free end of the tube 1 m from T_{0m} (SS0.05m).

The T-Chain was towed at a speed of less than 1 m s^{-1}, and because of the reduced speed T_{0m} (SS1m) sank to a depth of few tens of centimeters. Note, however, the good correspondence between the T-Chain interpolated surface temperature T_{0m} (Chain) and T_{0m} (SS0.05m) suggesting that the former indeed corresponded to the temperature in the first centimeters of the ocean. Because the depths of these three measurements cannot be determined precisely, they are all considered to be surface measurements and are assigned a depth of 0 m. During Palau2013 the R/V Mirai encountered a heavy rain event characterized by a rain rate reaching approximately 100 mm h^{-1} for more than half an hour (Figure 1c). During and after this event, the wind speed remained between 0 and 3 m s^{-1} and a strong surface cooling of several tenths of a degree was observed. The maximum temperature decrease was observed nearly 2 h after the rain event ended. Figure 1 also shows a time series of T_{int} and S_{int} (i.e., at the top of the salinity and temperature microlayer) and $T_{subskin}$ and $S_{subskin}$ (i.e., below the salinity and temperature microlayer) calculated by the present scheme with a bulk salinity taken to be 35 psu and a bulk temperature of 29.6°C corresponding to the temperature observed at a depth of 4 m immediately before the rain event. We set the extent of the rain-induced lens to be $r_0 = 10$ km based on radar observations of the size of the rain storm in the atmosphere. Just below the salinity microlayer, $S_{subskin}$ reaches its minimum at the end of the rain event with a drop of -3.5 psu. At the air-sea interface, S_{int} drops of almost -4 psu. Note that the freshening of the microlayer itself, which is $S_{int} - S_{subskin}$, reaches -1.2 psu during the rain event (not shown). On the other hand, temperature reaches its minimum 2 h after the rain ceased. This is partly due to the weakening of the wind around 2100 UTC but this lag between salinity and temperature minima is also seen when the scheme is run using constant wind speed. The reasons for the lag will be further discussed below when cases with idealized forcing are considered. The cool skin effect, seen as a -0.25°C difference between the model estimates for T_{int} and $T_{subskin}$ before the rain event, disappears during the rain event and reforms quickly after the rain stops. The maximum temperature decreases both at the interface and below the microlayer (subskin) during rain are, therefore, comparable (around -0.7°C). The high-frequency variations in temperature are not well captured by the scheme. This may be partly due to the fact that the dependence of the idealized profile on winds stronger than 2 m s^{-1} was limited by the parameterization. Additionally, the forcing observed by the ship may not necessarily reflect the forcing that resulted in the observed changes in temperature, since the ship was moving through the water and, therefore, the observations are a convolution

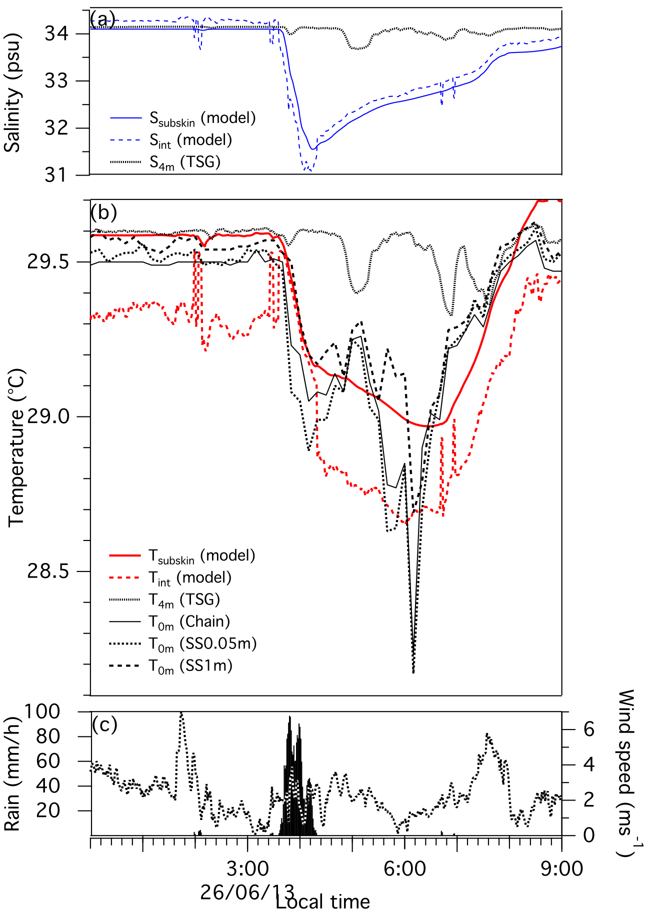

Figure 1. Data and modeling results from the Palau2013 cruise (135E, 12N) from 26 June 2013 (local time) showing rain-induced surface salinity decrease and cooling. (a) Model results of interface salinity, S_{int} (dashed blue line), and sub-skin salinity, $S_{subskin}$ (solid blue line), and foundation salinity measured by the ship's thermosalinograph (TSG) at a depth of 4 m, S_{4m} (dashed black line), during the rain even. (b) Model (red) and observational (black) results for temperature: The model results show the interface temperature, T_{int} (dashed red line), and the sub-skin temperature, $T_{subskin}$ (solid red line); The observational data are taken from the three different systems aboard the R/V Mirai, T_{4m} (TSG) is temperature measured by the ship's TSG at a depth of 4 m (black small dashed line), T_{0m} (Chain) is the surface temperature deduced from the temperature chain (black solid line), T_{0m} (SS0.05m) is the temperature from the 0.05-m sensor on the temperature snake (black medium dashed line), and T_{0m} (SS1m) is the temperature from the 1 m sensor on the temperature snake (black long dashed line). (c) Time series of the observed rain rate (solid line, mm h^{-1}) and wind speed (dashed line, m s^{-1}).

of temporal and spatial variability. However, the scheme reproduces the duration of the fresh lens event, and the modeled $T_{subskin}$ is comparable to the T_{0m} (SS0.05m) and T_{0m} (Chain).

In order to illustrate the dependency of the shape of upper ocean temperature profiles on the wind speed, Figure 2 shows a plot of profiles of the normalized temperature difference between temperature at depth z and temperature at a depth of 3 m (T_{3m} (Chain) – T_z (Chain))/(T_{0m} (Chain) $-$ T_{3m} (Chain)) as a function of wind speed. Note that the sign of the normalized difference is chosen in order to recall that we are considering a cooling of the near surface. The field data were collected using the T-Chain during the cooling event shown in Figure 1. The corresponding normalized idealized profiles, defined by (11) for a wind-dependent η as described in the preceding section and by $T_{-\delta}=T_{0m}$ (Chain) and $T_{-\delta}=T_{3m}$ (Chain) and normalized accordingly, are also superimposed. This is done in order to focus on the wind-dependent shape of the temperature profile assumed by the model to derive (14). Note that, for the sake of clarity of the figure, only cooling larger than -0.2°C is shown. Thermal stratification associated with the fresh lens are mainly within the top meter of the ocean and can reach ~0.5°C m^{-1} (not shown), consistent with previous observations [*Reverdin et al.*, 2012]. Although variability exists among T-chain profiles for comparable wind speeds, there is a tendency toward having shallower and steeper temperature gradients under weaker winds. The dependency of the idealized profiles shape η on the wind in (11) is an attempt to reproduce this tendency. However, for this rather limited wind speed interval (it spans from 2 to 2.5 ms^{-1}), the idealized profiles appear less sensitive to the wind. To further explore the results from this example, in the next section we present statistical results from idealized forcing experiments that will provide arguments in favor of the chosen function for the wind-dependent profile.

A second dataset that can be used for validating the scheme is provided by measurements made aboard the R/V Kilo Moana in December 2011 in the equatorial central Pacific Ocean [*Asher et al.*, 2014b] (hereafter referred to as KM-11). During KM-11, a Surface Salinity Profiler (SSP) was deployed during rain storms and measured salinity and temperature at depths of 0.11, 0.26, 1.04, and 2 m [*Asher et al.*, 2014b]. During a deployment on 14 December 2011, a rainstorm with rain rates of up to 60 mm h^{-1} associated with wind speeds as low as 1 m s^{-1} lasting 30 min was encountered [*Asher et al.*, 2014b]. As assumed by

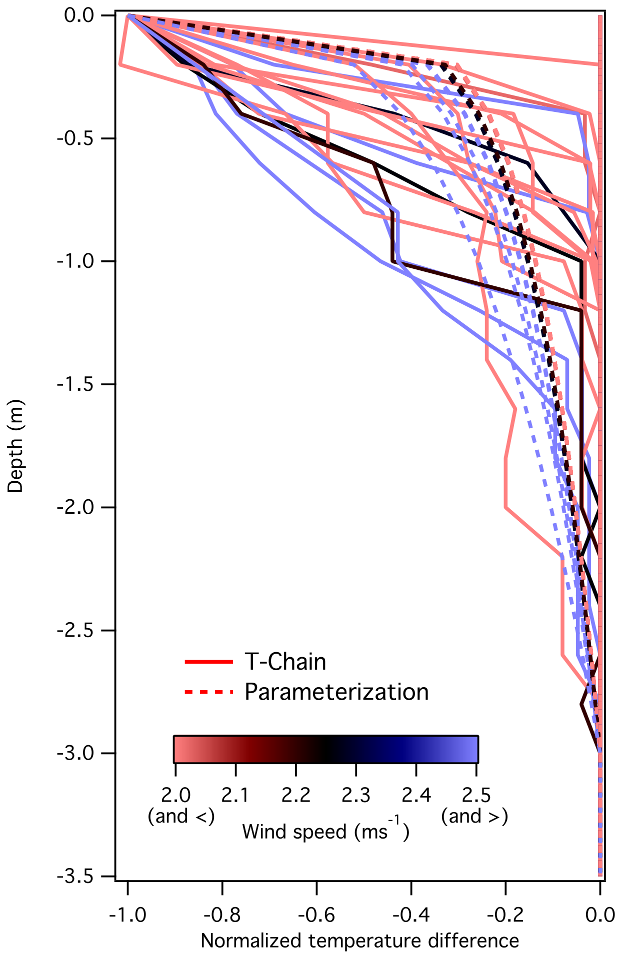

Figure 2. Profiles of normalized temperature differences (T_{3m} (Chain) − T_z (Chain))/(T_{0m} (Chain) − T_{3m} (Chain)) observed from R/V Mirai by the Thermistor chain (T-Chain, solid) during the cooling event of 25 June 2013 (19–22 h) near Palau and corresponding wind-dependent idealized profiles compute using (11) with the constraint of having the same temperature as observed at 0 and 3 m depths (dashed). Only profiles with a surface cooling of more than −0.2°C are retained here. Color represents the wind speed (in m s^{-1}).

Drushka et al. [2016], the data from this event can be used to generate a time series showing the evolution of a fresh lens that can be used to validate the present scheme.

Figure 3 shows temperature and salinity data from the SSP used during KM-11 along with model results for this same event where the model was initialized using the environmental forcing shown in Figure 3c. The SSP data show that both salinity and temperature at 0.11 m depth, $S_{0.11m}$ (SSP) and $T_{0.11m}$ (SSP), respectively, decrease rapidly at the onset of the rain, and the minimum in either $S_{0.11m}$ (SSP) or $T_{0.11m}$ (SSP) occurs a few minutes after the maximum value of R. This rapid decrease in salinity is seen in the model results for the sub-skin salinity, $S_{subskin}$ (Model) predicted by (14). Although $S_{subskin}$ corresponds to a depth of at most a millimeter and should, therefore, show a larger variation than $S_{0.11m}$, the sub-skin salinity decrease predicted by (14) underestimates the minimum value of $S_{0.11m}$ (SSP) with the largest decrease in $S_{subskin}$ (Model) being −0.75 psu compared to a decrease of −1.13 psu for $S_{0.11m}$ (SSP). Additionally, the decrease in S_{int} (Model) precedes the decrease in $S_{0.11m}$ (SSP) and $S_{subskin}$ (Model). This behavior might be expected as the thin microlayer reacts faster to the addition of freshwater than the deeper lens.

In contrast to the results for salinity, the observational and modeled results for temperature do not show good agreement between the interface and sub-skin temperatures from the model, T_{int} and $T_{subskin}$ (Model), and temperature measured by the SSP at 0.11 m, $T_{0.11m}$ (SSP). The decrease in both T_{int} (Model) and the modeled sub-skin temperature, $T_{subskin}$ (Model), is smaller and does not occur as rapidly as the cooling shown in $T_{0.11m}$ (SSP). The modeled temperature decrease at the surface is limited by the increase of the wind after 1315, which mixes the cooler and fresher surface water with the warmer higher salinity water below.

Part of these differences between the measured and modeled time series of salinity and temperature may be explained by the fact that the observed precipitation and wind may not correspond to the forcing that led to the observed lens formation. In other words, the rain rate measured at a particular location is not necessarily the same rain rate that deposited the freshwater measured at a particular depth. Additionally, as discussed by *Drushka et al*. [2016], the Taylor hypothesis used to turn the spatial data from the SSP into a time series might exacerbate this problem.

Another possible source of discrepancy is the sensitivity of the shape of salinity and temperature profiles (11) to wind speed through η, which appears in (14). As η decreases, salinity and temperature gradients become steeper and shallower and the variations of $T_{subskin}$ and $S_{subskin}$ are larger for a given rain event. Figure 4 shows the salinity and temperature profiles observed by the SSP during the same event shown in Figure 3. In order to visualize the effect of wind speed on the shape of the profiles, Figure 4 shows wind-

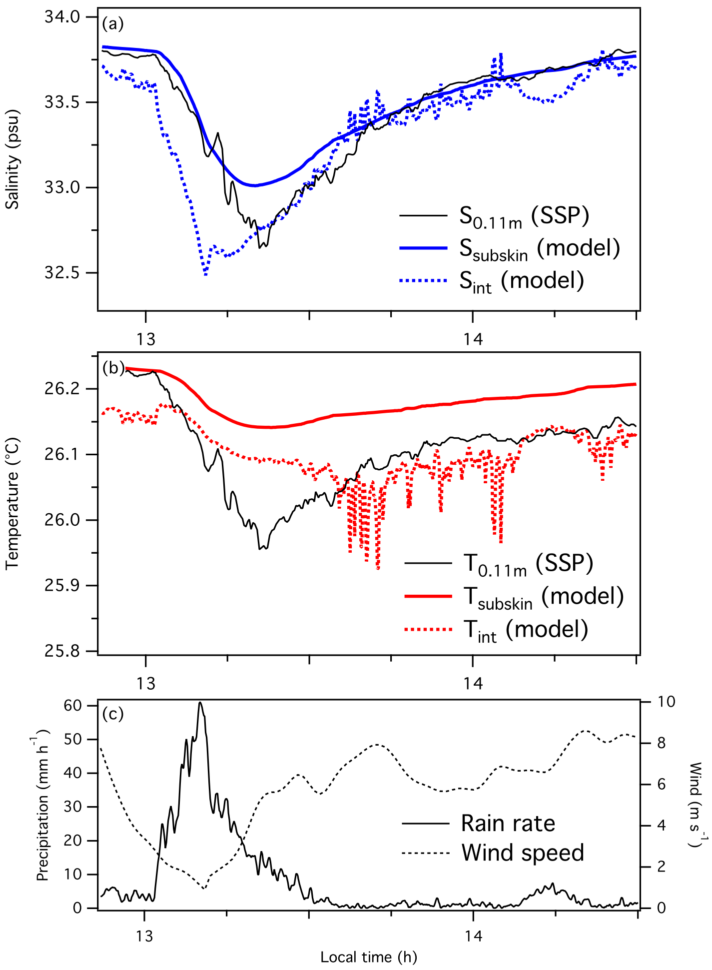

Figure 3. Rain-induced freshening and surface cooling as observed at a depth of 0.11 m on 14 December 2011 by the SSP during KM11 cruise and the corresponding results from the model. a (resp. b) Shows the results for salinity, where the black solid line is salinity (resp. temperature) at 0.11 m measured by the SSP, $S_{0.11\text{m}}$ (SSP) (resp. $T_{0.11\text{m}}$), the blue (resp. red) solid line is the sub-skin salinity (resp. temperature) calculated using (14), S_{subskin} (model) (resp. T_{subskin}) and the blue (resp. red) dashed line is salinity (temperature) at interface, S_{int} (model) (resp. T_{int}). (c) Shows rain rate (solid black line) and wind speed (dashed blue line).

dependent idealized profiles computed from (11) by imposing the condition that the values at 2 m and 0.11 m are equal to the SSP measurements. Observed and idealized profiles are then normalized by the difference between 2 m and the extrapolated subskin value from the idealized profile. This allows comparing the shape of the profiles in the 2 first meters of the ocean as a function of wind speed.

The first feature is that normalized profiles of both observed salinity and temperature are similar. This provides strong evidence that the evolution of both parameters can be treated using a common idealized profile for a given set of conditions. As seen for the Palau2013 case, the wind-dependent idealized profile used in the scheme shows less variability than is observed. Specifically, the scheme overpredicts the stratification in high winds (red colors). On the other hand, the scheme produces unrealistically weak stratification near the surface in weak winds (blue colors). This suggests that our choice to limit the dependency of η to wind above 2 m s^{-1} may lead us to underestimate the impact of rainfall on T and S in weak wind conditions. However, attempts to change the wind dependence of η to get better agreement in this case reduces the statistical agreement between our scheme and the GOTM results in the idealized context (see next section). This suggests that additional observational data, particularly in the upper 10 cm, are needed to further refine the wind dependency of η.

3.2. Idealized Forcing

Figure 5a shows time series for interface and sub-skin temperature and salinity calculated using the scheme in equation (2) and (14) assuming the idealized forcing shown in Figure 5b. The conditions are identical to those used by *Drushka et al.* [2016], where U was constant at 2 m s^{-1}; air temperature, T_{air}, was constant at 23.95°C; RH, was constant at 83.3%; the foundation ocean temperature, T_{fnd} was constant at 26.53°C; the foundation salinity, S_{fnd} was constant at 34.1 psu; and cloud cover was assumed to be 100% [*Drushka et al.*, 2016]. Following *Drushka et al.* [2016], the rain event is Gaussian-shaped with respect to time, with a duration of 1 h (defined as the length of time for which R is more than one tenths of its maximum value) and has a maximum rain rate, R_{max}, of 50 mm h^{-1}. The simulation begins at sundown, local time, with the rain event beginning 1 h after the beginning of the run.

The salinity and temperature time series in Figure 5a show that a fresh and cool lens forms under rain that persists for 8 h until it dissipates at t = 9 h. After sunrise at t = 12 h a weak diurnal warming of about 0.4°C

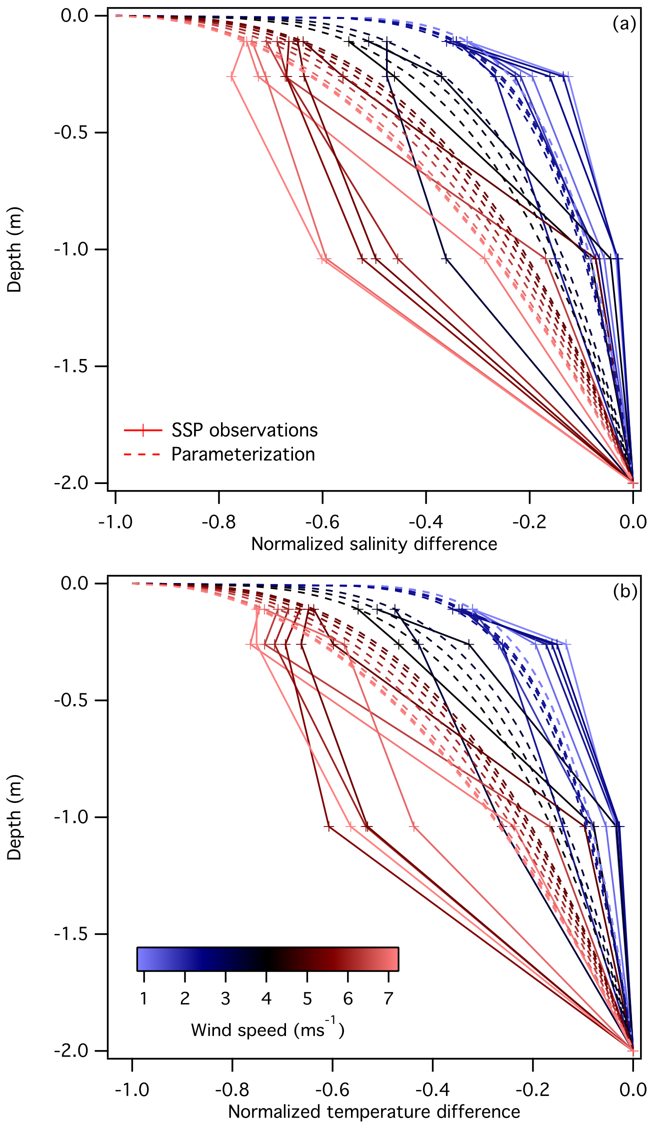

Figure 4. Profiles of (a) salinity and (b) temperature differences between the surface and a depth of 2 m. Observational data (pluses and solid lines) are taken on 14 December 2011 during KM11 and the corresponding wind-dependent idealized profiles (dashed lines) are calculated using (11) and imposing their values at 0.11 and 2 m depth to be the same as the observations. The observed and idealized profiles are then normalized by the difference between the surface (from the idealized profiles) and 2 m depth. The color of the line denotes the wind speed (color scale shown on the figure) and the profiles shown are taken at 2 min intervals from 1300 to 1330.

occurs due to the downwelling shortwave radiation. Therefore, the general features produced by the scheme for these idealized conditions are consistent with previous modeling and observational studies.

During the rain event, the near-surface sub-skin salinity drops by approximately 2.5 psu before recovering, whereas temperature continues to decrease after the rain stops, reaching a minimum of $-0.75°C$ due to cooling from the net upward longwave radiation and sensible/latent heat fluxes. This lag between salinity and temperature minima associated with rainfall and also shown in Figure 1, is consistent with the observations. Its origin has been explained by *Reverdin et al.* [2012]. However, as will be discussed below, the lag only exists for light wind conditions.

In the absence of the freshwater input from rain, Figure 5a shows that S_{int} is saltier than $S_{subskin}$ by 0.2 psu due to surface evaporation. In the presence of rain, S_{int} is fresher by up to 0.6 psu. This is less than the 4% freshening of the microlayer computed by *Schlussel et al.* [1997] based on renewal theory for a rain event observed during TOGA-COARE. However, the decrease in $S_{subskin}$ in Figure 5a is comparable to the decrease in $S_{0.02}$ measured by *Paulson and Lagerloef* [1993] during TOGA-COARE. T_{int} is lower than $T_{subskin}$ by about 0.3°C except during rain, when the rain-induced surface mixing [*Schlussel et al.*, 1997] homogenizes the water surface. This warming of T_{int} during rain as shown in Figure 5a explains why there is a slight increase in the sensible and latent heat flux between 1 and 2 h of the run (see Figure 5b).

In order to compare the result of our model to the *Drushka et al.* [2016] results, we now show statistics of variations of $X_{subskin} - X_{fnd}$ as no diagnostic for the variation of T and S in the skin layer is included in their results. Figure 6 shows the maximum salinity decrease between the subskin and foundation salinities, ΔS_{max}, the maximum temperature decrease between the subskin and foundation temperature, ΔT_{max}, and lifetime of fresh lenses as a function of U and R_{max} as calculated using the scheme in (14) for the idealized environmental and forcing conditions given in Figure 5 (i.e., T_{air}, RH, S_{fnd}, and T_{fnd} were the same as in Figure 5, along with the lifetime of the rain event). ΔS_{max} and ΔT_{max} are shown for $1 \text{ m s}^{-1} \leq U \leq 10 \text{ m s}^{-1}$ and $R = 2 \text{ mm h}^{-1}$, $R = 5 \text{ mm h}^{-1}$, $R = 10 \text{ mm h}^{-1}$, $R = 50 \text{ mm h}^{-1}$, and $R = 80 \text{ mm h}^{-1}$, Also shown in Figure 6a is the parameterization of ΔS_{max} in terms of U, and R developed by *Drushka et al.* [2016] for $2 \text{ m s}^{-1} \leq U \leq 10 \text{ m s}^{-1}$ and $R = 2 \text{ mm h}^{-1}$, $R = 5 \text{ mm h}^{-1}$, $R = 10 \text{ mm h}^{-1}$, $R = 50 \text{ mm h}^{-1}$ extended for $U = 1 \text{ m s}^{-1}$ and $R = 80 \text{ mm h}^{-1}$.

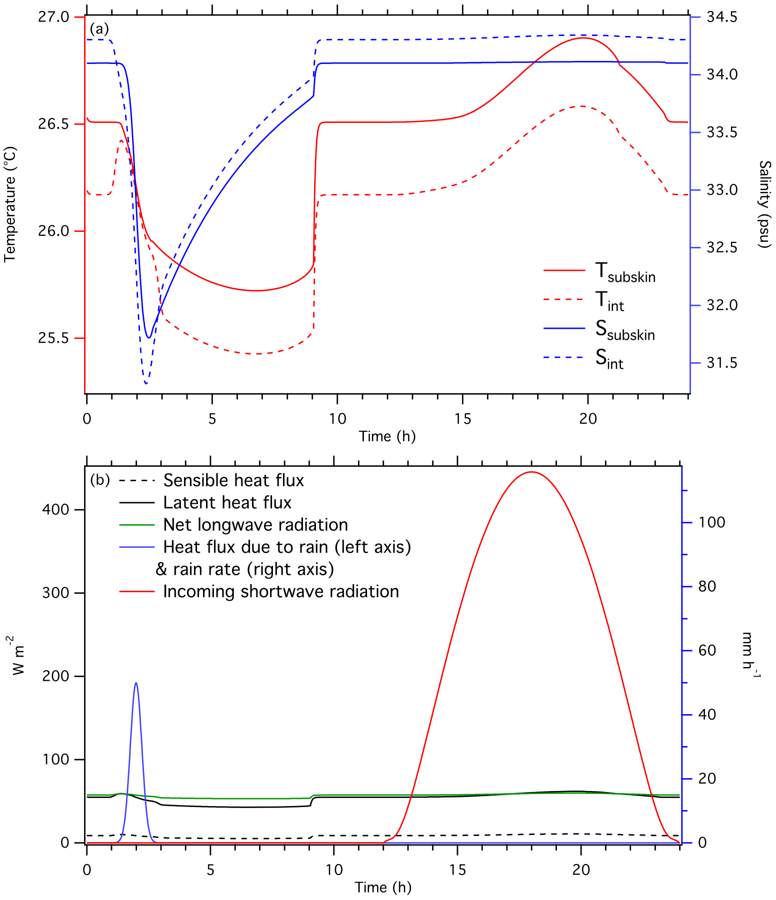

Figure 5. (a) Skin and sub-skin temperature and salinity predicted by the scheme in equation (14) when forced by a set of idealized conditions used by *Drushka et al.* [2016] with the heat fluxes and rain rates shown in (b) (note that the sign of the downwelling shortwave flux is opposite the sign of the latent, sensible, and longwave fluxes). The rain event assumes a Gaussian distribution of rain rate with respect to time with a maximum rate, $R_{max} = 50$ mm h^{-1}, and a time constant of 1 h. The heat fluxes were calculated assuming a constant air temperature of 23.95°C, RH of 83.3%, bulk ocean temperature of 26.53°C, salinity of 34.1 psu, and wind speed of 2 m s^{-1} [*Drushka et al.*, 2016].

In the case of salinity, ΔS_{max} values and the lifetime of the fresh lenses shown in Figure 6 are comparable to the salinity decreases calculated by *Drushka et al.* [2016], as shown by the agreement between their parameterizations shown in Figure 6a and the results from the scheme. Similarly, comparison of the lens lifetimes calculated by the scheme with those reported by *Drushka et al.* [2016] (see their Figure 5) with the results in Figure 6c shows similar order of magnitudes in the estimated lifetimes. One significant difference between the ΔS_{max} values calculated by *Drushka et al.* [2016] using GOTM and the ΔS_{max} values from the scheme is that for the latter, ΔS_{max} is smaller for a given R_{max} at higher wind speeds, a result that is consistent with the KM-11 case shown in Figure 3. This could be due to the simple wind-dependency chosen for η in (11). The analysis of a larger amount of observations of rain-induced stratification with different wind conditions is, however, necessary to better constrain this dependency. A second difference is that the lens lifetime calculated by the present scheme when wind speed and rain rate are low are smaller than the lifetimes calculated by *Drushka et al.* [2016]. The longer lifetimes seen by *Drushka et al.* [2016] might be due to the stabilizing effect of solar radiation as rainfall in their simulations was modeled to occur at 0900 local time whereas the simulations reported here used rainfall beginning 1 h after sundown. This will be discussed further in the next section.

ΔT_{max} shows a large sensitivity to U and R_{max} as it ranges from a few tenths of a degree up to 2°C for weak winds and high rain rates. Therefore, surface cooling associated with fresh lenses as calculated by this scheme can be on the same order of magnitude, although reversed in sign, as the diurnal warming caused by the downwelling shortwave radiation [e.g., *Takaya et al.*, 2010]. Furthermore, the lifetime of these cooling events is comparable to the timescales of diurnal warm layers (several hours up to a day).

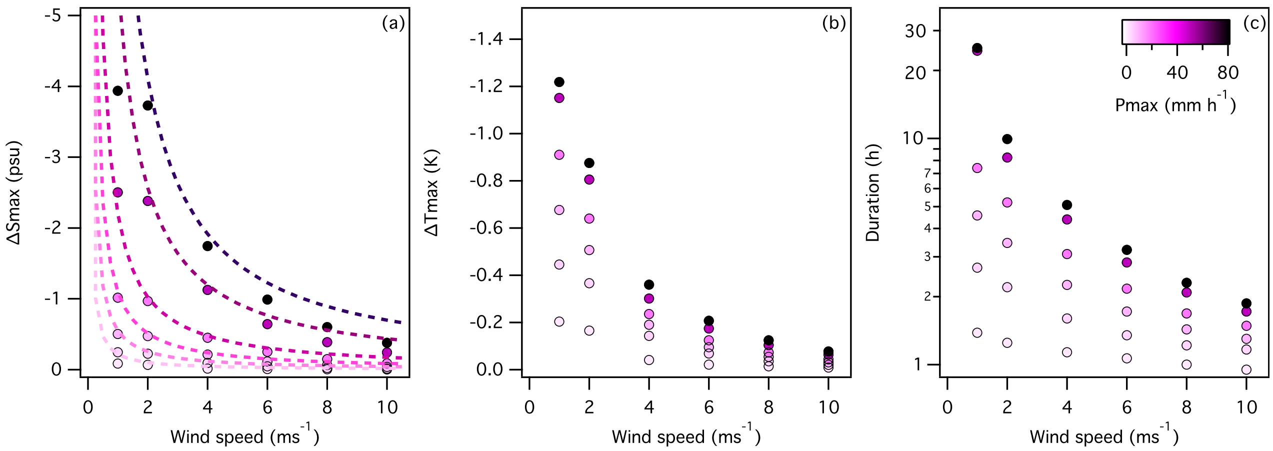

Figure 6. Sensitivity of (a) the sub-skin salinity drop (ΔSmax, psu), (b) the sub-skin temperature drop (ΔTmax, °C), and (c) the duration of the freshwater cool lens (h) to the wind speed and to the peak precipitation Pmax (colors, duration of each rainy event is 2 h) in idealized simulations. The peak rainfall chosen as $P_{max} = 2, 5, 10, 20, 50$, and 80 mm h^{-1}. The temperature and salinity drops are evaluated just beneath the diffusive microlayer. Apart from rain rate and wind, the other boundary conditions are kept unchanged (see Figure 5). Dashed lines on (a) are the fit from *Drushka et al*. [2016] given in their equation (1).

Figure 7 shows a scatter plot of $\Delta S_{\max}$ versus $\Delta T_{\max}$ calculated as a function of U and R_{max} across the depth differences, namely interface–foundation (triangles), subskin–foundation (circles) and 0.15 m–foundation (squares). The results show that the microlayer mostly impacts maximum salinity variations and only marginally the corresponding maximum temperature drops. This can be understood by considering Figures (1 and 3), and 5: temperature reaches its minimum after rain ceased and when the cool skin has already reappeared, whereas salinity at the interface and underneath decreases roughly in phase during the rain event so their effects add up. This scatter plot further shows drops in temperature and salinity at 15 cm depth that can be compared to observations by *Reverdin et al*. [2012] and in particular their Figure 8. These near-surface variations span the range of observed values and have a comparable relationship to the forcing, for instance, with a decrease of −2 psu corresponding to a cooling of about −0.6°C in moderate wind conditions.

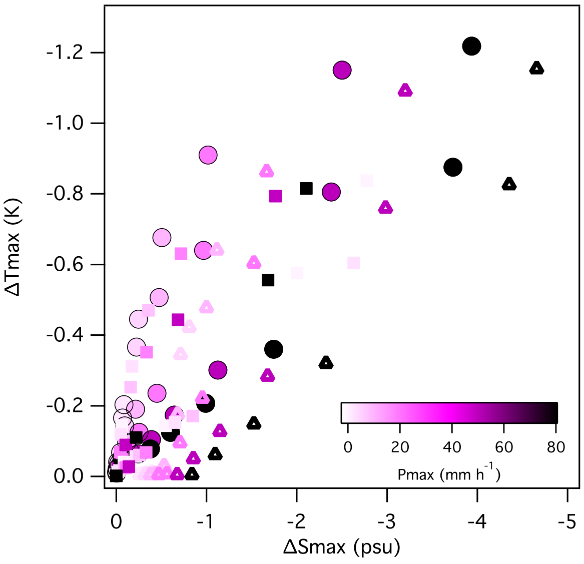

Figure 7. Temperature drops as a function of salinity drops at the sea interface (triangles) and just below the diffusive microlayer (sub-skin, circles) and at 15 cm depth (squares) in the idealized forcing computations. Colors represent the peak rain rate.

3.3. Scheme Sensitivity

Drushka et al. [2016] showed that for a given total amount of rainfall the lifetime and magnitude of the decrease in surface salinity of a surface freshening event is a function of both the duration of the rain event and $R_{\max}$. This implies that surface freshening events and temperature decreases predicted using rain rates from a relatively low temporal resolution time series of precipitation such as the 3-hourly CMORPH data might not capture the full range of variability in surface freshening that would be seen in the ocean. Figure 8 shows the results from computations similar to those performed by *Drushka et al*. [2016] for surface wind speeds of 4 m s^{-1} and 9 m s^{-1}. The present simplified scheme also exhibits such behavior for salinity with decreases ranging from −0.4 to −1.1 psu for a wind of 4 m s^{-1} and from −0.025 psu to 0.45 psu for a wind of 9 m s^{-1} as $R_{\max}$ increases from 10 mm h^{-1} to 100 mm h^{-1} (Figures 8b and 8e).

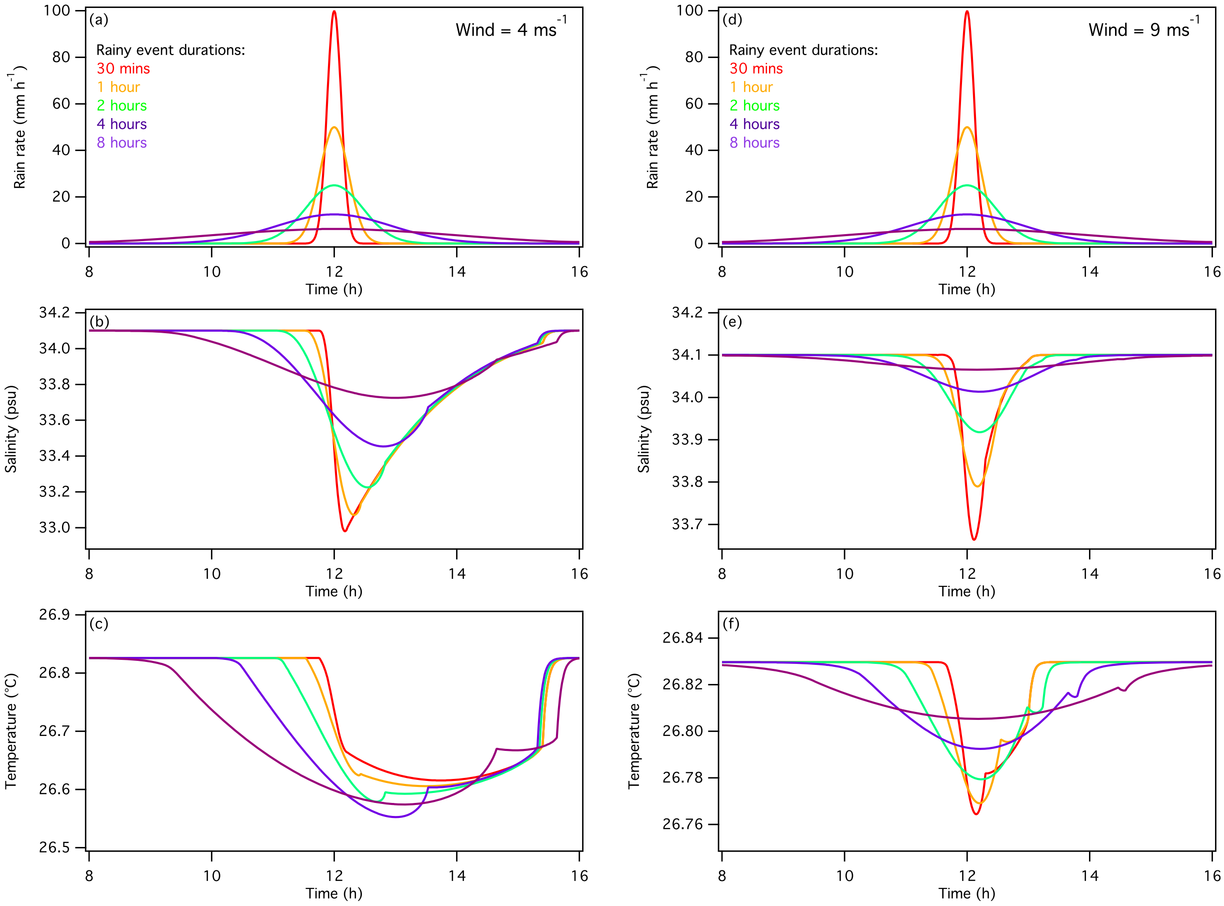

Figure 8. The effect of wind and the temporal distribution of rain rate on the magnitude and lifetime of the sub-sin freshening and cooling caused by rain. The rain in these simulations was characterized by the same amount of accumulated rainfall, but that total accumulated over durations ranging from 0.5 to 8 h following a Gaussian distribution for rain rate with respect to time. Results for wind speeds of 4 m s^{-1} (a) and 9 m s^{-1} (d) and the result for sub-skin salinity (be) and temperature (cf).

In contrast to salinity, the temperature response as a function of R_{max} and wind speed is more complicated (Figures 8c and 8f). For stronger wind speed such as $U = 9$ m s^{-1} (Figure 8f), the cooling is mainly due to the rain-induced sensible cooling. This is seen by the temperature evolution being roughly in phase with the evolution of salinity and the amplitude of the change in both temperature and salinity increasing with increasing R_{max}. In contrast, under light wind conditions (Figure 8c), the cooling at the surface is mainly due to the surface fluxes acting on the stable fresh lens during and after the rainy event. This is seen by the decrease in correlation between the temperature and salinity changes, where the temperature change reaches its maximum value after the maximum change in salinity. Furthermore, the temperature decrease is larger for rain events with longer duration, where the longer lifetime of the stable surface stratification provides more time for the surface heat fluxes to cool the fresh lens. Therefore, increasing the rainy event duration and decreasing R_{max} work to increase the magnitude of the temperature change. The switch between these two regimes for temperature evolution gradually occurs when wind speed varies from 4 m s^{-1} to 9 m s^{-1}.

The scheme was also used to study the effect of the downwelling shortwave radiative flux on the lifetime and temperature structure of these fresh lenses. Figure 9 is similar to Figure 6 and shows ΔS_{max}, ΔT_{max}, and lifetime of fresh lenses as a function of U and R_{max} as calculated using the scheme in (14) for the idealized environmental and forcing conditions given in Figure 5. However, in Figure 9, the calculations were performed for daylight from 0 to 12 h rather than from 12 to 24 h as in Figure 5b, keeping the peak downwelling shortwave radiative flux the same as in for Figure 6.

Comparing the results in Figure 9a with Figure 6a shows that the change in temporal phase of the shortwave radiative flux with respect to the time when R_{max} occurs has no impact on ΔS_{max}. In contrast, comparing the results in Figure 9b with the results in Figure 6b shows that ΔT_{max} is a few tenths of a degree

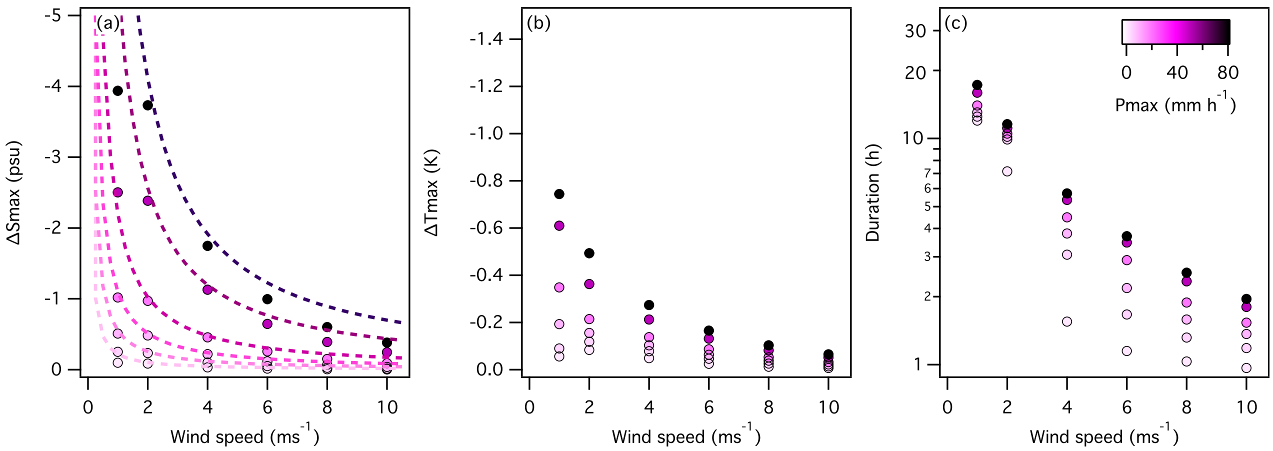

Figure 9. As Figure 6 but during day (shortwave has the same magnitude as in Figure 5b but peaks at 6 h).

smaller for all U and R_{max}. This effect of the shortwave flux on ΔT_{max} has been observed for rain-produced fresh lenses as reported by *Reverdin et al.* [2012]. Comparison of Figure 9c with Figure 6c shows that the shortwave radiative flux also affects the lifetime of a rain-generated fresh lens, with lifetimes being longer for fresh lenses generated by daytime rain events when wind speeds are small.

This increase in lifetime is most likely due to the interplay between the lack of mechanical mixing due to wind stress and the increase in buoyancy due to the shortwave-induced surface warming. At night, when there is no warming and wind speeds are low, the upward surface heat flux cools the fresh lens until the density stratification due to the decrease in salinity is no longer stable. During the daytime, the shortwave flux acts to offset this cooling and depending on the net heat flux (sum of the latent, sensible, longwave, and shortwave fluxes) the lens either takes longer to cool or a warm, fresh lens may form. In this latter case, the fresh lens will dissipate after sunset when the net heat flux reverses sign and the surface cools enough to destratify. In fact, the GOTM results presented by *Drushka et al.* [2016] show this effect for light rains and 2 m s^{-1} wind. Finally, note that in this scheme, the effect of morning rainfall on the maximal temperature associated with the developing diurnal warm layer discussed by *Webster et al.* [1996] is not reproduced (not shown).

The choice of d (see equation (11)) has a large impact on ΔS_{max} and ΔT_{max} that are calculated using the scheme. For instance, if $d = 10$ m instead of $d = 3$ m as assumed for the results presented above, the magnitude of ΔS_{max} and ΔT_{max} would be strongly reduced. Furthermore, the use of a constant η in (11) results in a linear relationship between either ΔS_{max} or ΔT_{max} and U instead of the power law obtained by *Drushka et al.* [2016].

The most appropriate values of d and η to be used in the scheme will have to be constrained with more in situ observations of surface fresh lenses. These observations should become available as a result of the two field campaigns that are part of the SPURS-2 program, the first conducted in the summer of 2016 and the second planned for the fall of 2017 [*Lindstrom et al.*, 2015]. Finally, although the effects of surface waves on fresh lenses are not taken into account in the results presented above, the COARE3 flux algorithm, which includes surface waves in the computation of the oceanic roughness parameters [*Fairall et al.*, 2003], was tested in the scheme. Although the results of these simulations are not shown, the effect of waves on roughness were found to have negligible impact on ΔS_{max}, ΔT_{max}, and lens lifetime.

4. Impact of Fresh, Cool Lenses on Ocean Surface Properties

The scheme was used to illustrate the potential impact of cool fresh lenses on both the monthly mean properties and the variability of ocean surface temperature and salinity. The scheme was used to model S and T in the equatorial western Pacific Ocean, which is one of the rainiest oceanic regions and is also characterized by weak surface winds. This region provides an end-member in terms of the impact of fresh lenses. Skin and near-surface salinity and temperature were computed using the scheme. Following *Drushka et al.* [2016], the scheme was forced using precipitation taken from the 3-h CMORPH dataset and the 6-h ERA-Interim wind speeds, RH, air temperature, and air pressure. Foundation temperature and salinity values

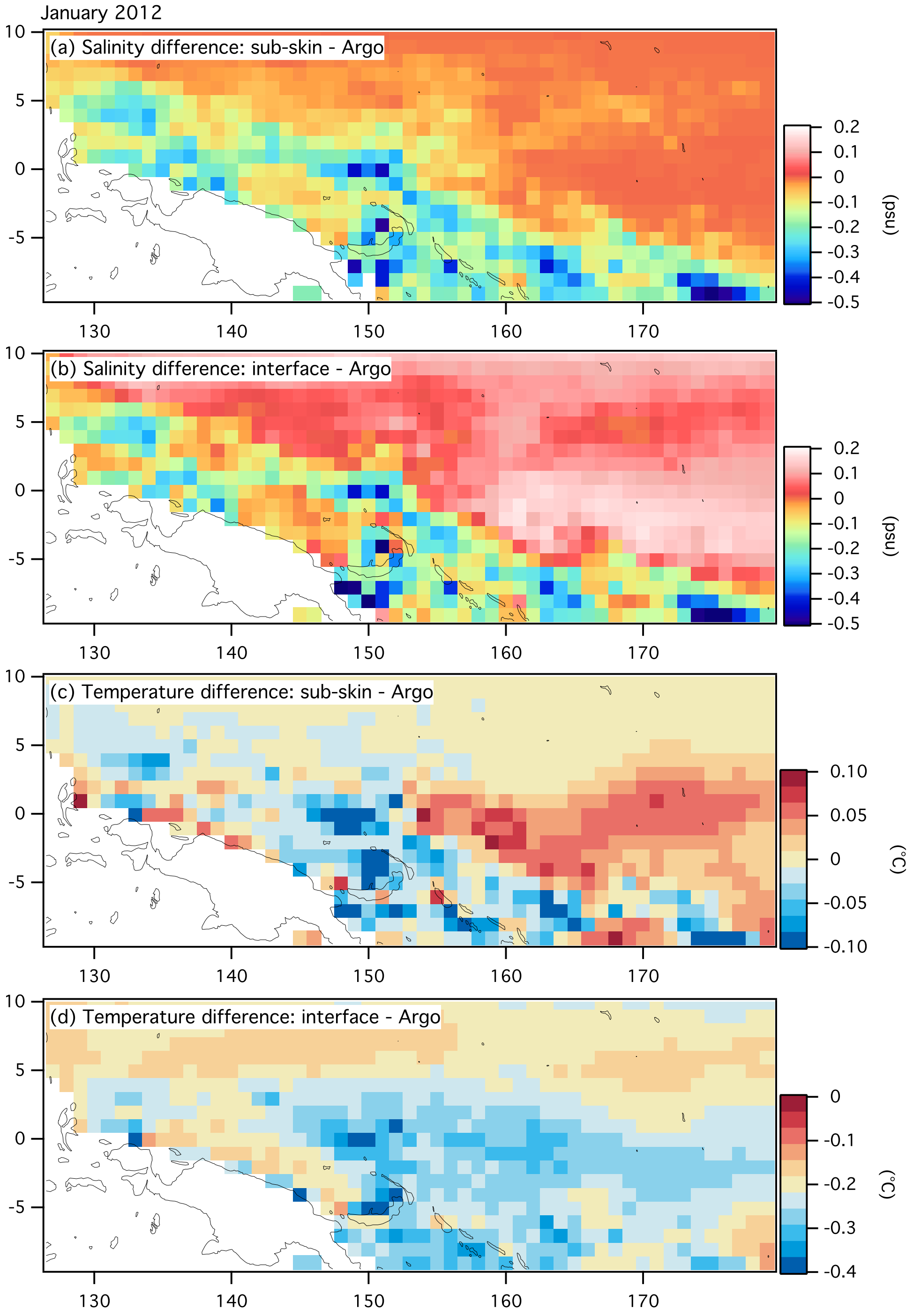

Figure 10. Average monthly difference between (a) and (c) sub-skin and 5 m-depth Argo observations and (b) and (d) interface and 5 m-depth Argo observations of (a) and (b) salinity (psu) and (c) and (d) temperature (°C) for January 2012.

were taken from monthly Argo observations and interpolated weekly. As shown above, all other conditions being equal, the characteristics of the freshwater lens depend on both R_{max} and the rain duration (see Figure 8). This implies that the skin and near-surface salinities and temperatures produced by the scheme during these simulations serve mainly to illustrate the effect of fresh, cool lenses on ocean surface properties.

Figure 10 shows spatial distribution of the difference between the foundation salinity (or temperature) as defined by the slowly varying Argo observations from a depth of 5 m and the monthly averaged sub-skin or

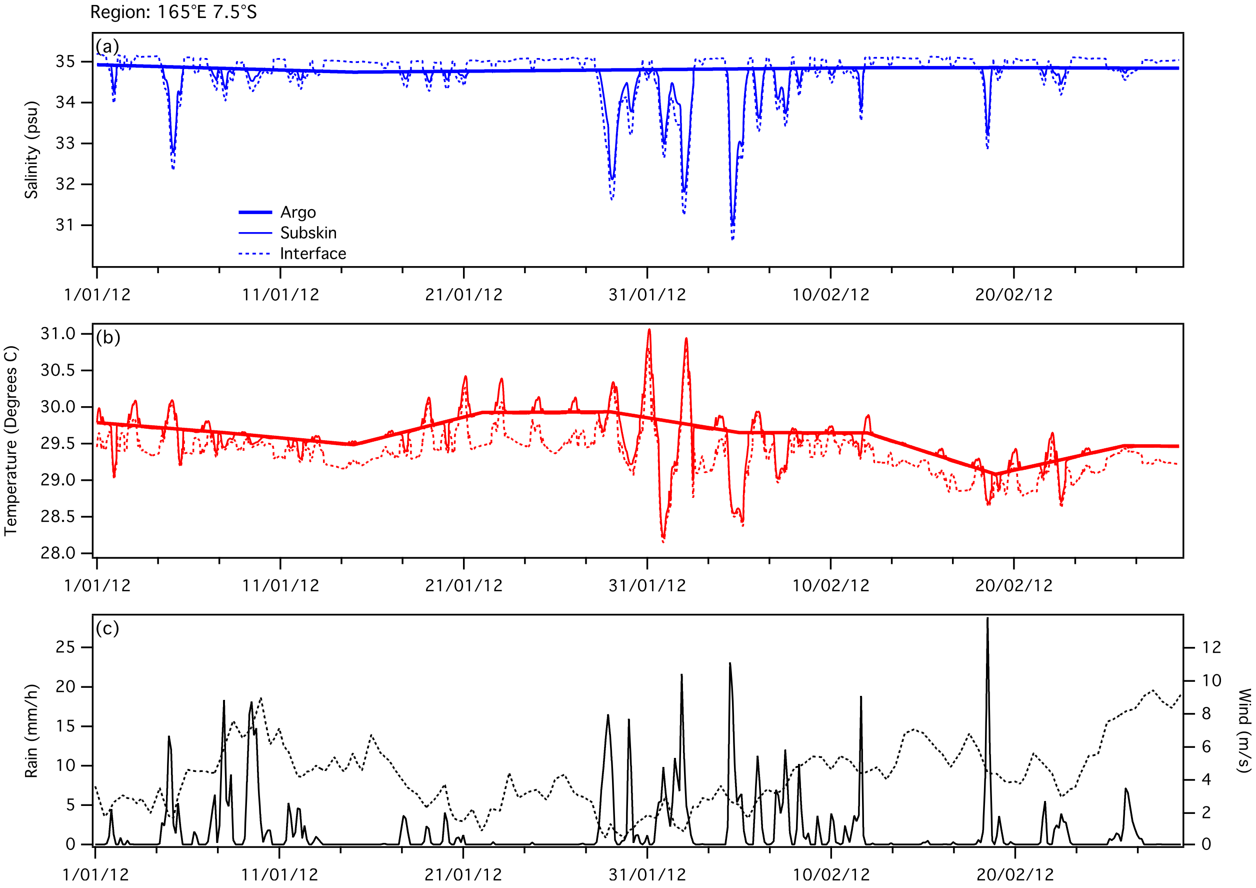

Figure 11. Time series of (a) salinity (blue, psu) and (b) temperature (red, °C) from Argo (linearly interpolated in time, thick), sub-skin (solid) and of the ocean interface (dashed) for the first 2 months of 2012 at 165E–7.5S, and (c) CMORPH precipitation (solid) and ERA0-Interim winds (dashed).

interface salinity (or temperature) calculated by the scheme for January 2012. Figure 11 provides 2-month long time series of the foundation salinity (from Argo), sub-skin salinity (from scheme), interface salinity (from scheme), foundation temperature (from Argo), sub-scheme temperature (from scheme), and interface temperature (from scheme) for the 0.5-degree by 0.5-degree region centered at 7.5 S, 165 E. Figure 12 shows the frequency distribution of the same parameters for the same region for the entire year 2012. Also shown in Figure 12 are frequency distributions of the difference between the latent (or sensible) heat flux calculated using interface temperatures from the scheme and latent (or sensible) heat flux calculated using the linearly interpolated Argo temperatures for the same time span and location as the salinity and temperature frequency distributions.

Figure 10a shows that the sub-skin salinity from below the microlayer is fresher on average than the Argo observations by a few tenths of a psu, with the largest freshening mostly corresponding to warm pool areas with larger mean rain rates and weaker mean winds (not shown). Interestingly, the spatial inhomogeneity of precipitation leads to large spatial variability in the surface freshening even in these monthly mean differences. Figure 10b shows an increased contrast between the rainy warm pool region and the region to the northeast. The northeast region is characterized by higher evaporation rates and a positive salinity difference across the diffusive microlayer.

The spatial variability of the precipitation is also visible in the difference between the mean subskin and Argo temperatures shown in Figure 10c. In the warm pool, this difference can reach -0.1°C. Note that the effect on temperature is offset by diurnal warming at these regions, which also correspond to weak wind conditions. Interestingly, the diurnal warming signal dominates near the Equator east of 155E. This shows how near-surface stratification due to diurnal warming and rainfall can impact large-scale horizontal surface temperature gradients that are important for large-scale mean circulation and variability modes such as El

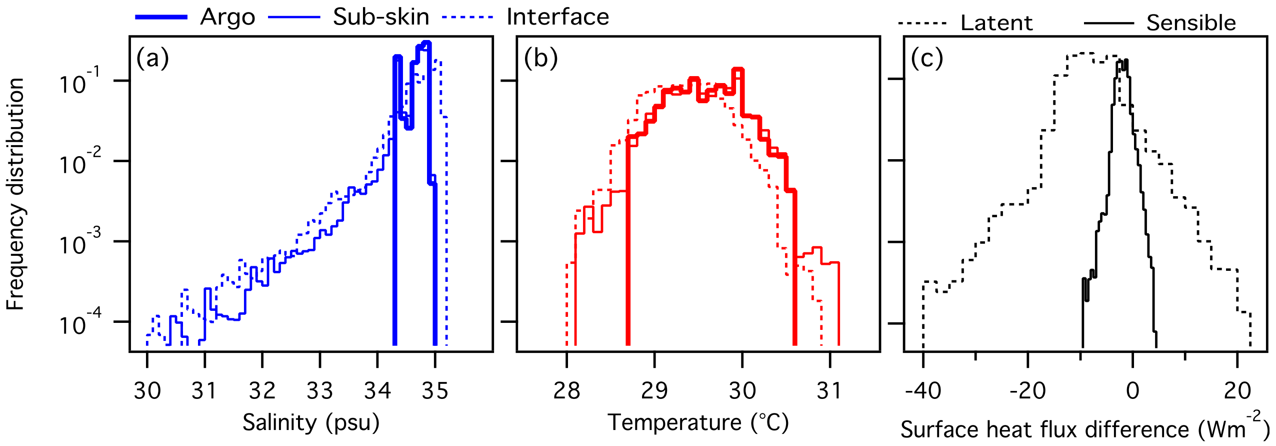

Figure 12. Frequency distribution of (a) salinity (blue) and (b) temperature (red) from Argo (linearly interpolated in time, thick solid), sub-skin (solid) and interface (dashed) for the year 2012 in 165E–7.5S, and of (c) the difference between latent (dashed) and sensible (solid) heat fluxes computed using the skin temperature and using linear interpolation of Argo observations.

Nino Southern Oscillation. However, when taking into account the skin effect (Figure 10d), this contrast disappears. The mean temperature difference between the interface and Argo observations primarily reflects the horizontal distribution of the cool skin effect that is mainly linked with the mean wind geographical distribution (not shown).

The corresponding temporal variability is illustrated in Figure 11 for a particular region of the warm pool (165E–7.5S). During the time period shown, several rain events occurred with maximum rain rates reaching 25 mm h^{-1} and rain duration exceeding 1 day on occasion. Their impact on S and T is clearly dependent on the wind speed. Note that the salinity decreases associated with these rain events have longer persistence times but similar magnitudes to salinity decreases observed during TOGA-COARE [*Paulson and Lagerloef*, 1993; *Schlussel et al.*, 1997]. Salinity and temperature variations are mostly due to the near-surface (subskin) variations. For instance, the modeled change in salinity across the microlayer does not exceed 1 psu whereas the difference between subskin salinity and Argo value can be several psu.

Based on the results in Figure 11, freshwater lenses are clearly a source of high frequency variability for T and S. However, in the case of T, the impact on longer timescales is offset by the presence of diurnal warming for comparable weak wind situations. This is particularly clear on 31 January for instance. The impact of rain-induced lenses on the variability of oceanic surface conditions is further characterized in Figure 12. The main impact of the skin microlayer is an enhancement of the surface salinity in the absence of rain (Figures 11a and 12a), and a shift of few tenths of a degree in the temperature distribution corresponding to the almost constant cool skin effect (Figure 12b). Near-surface stratification induced by rain significantly impacts surface salinity (Figure 12a), and in this case the associated cooling effect overcomes diurnal warming (Figure 12b). Figure 12c illustrates the associated impact on surface heat fluxes. The skin effect accounts for the fact that the distributions are centered on negative values: -1 W m^{-2} for the sensible heat flux and about -10 W m^{-2} for the latent heat flux. The impact of rain-induced lenses on heat fluxes is comparable to the impact of diurnal warming and can reach several tens of Wm^{-2} in absolute value for the latent heat fluxes and up to -10 W m^{-2} for the sensible heat flux.

5. Summary and Discussion

Freshwater cool lenses that form under rain [e.g., *Reverdin et al.*, 2012; *Asher et al.*, 2014b; *Drushka et al.*, 2016] are light wind phenomena, analogous to diurnal warm layers in that rain creates a stable surface density stratification similar to the one that is created by the heating due to shortwave solar radiation. Because of this similarity, it is possible to describe the spatial and temporal evolution of a stable near-surface density stratification caused either by salinity decreases or temperature increases with a common framework. The prognostic model of *Zeng and Beljaars* [2005] for diurnal warm layers was extended to represent cooling associated with rain-induced fresh lenses by taking into account the concomitant evolution of near-surface salinity. The prognostic model also accounts for the effect of the freshwater flux on density, the surface mixing due to the additional surface stress due to rain [*Caldwell and Elliott*, 1971], and the rain-induced sensible heat flux [*Gosnell et al*., 1995]. A resolution-dependent spreading term based on a gravity current box model [*Fay*, 1969; *Huppert and Simpson*, 1980] was added to the scheme to parameterize the gravity-induced horizontal spreading. Finally, because the properties of the surface microlayer are critical in determining air-sea fluxes of heat and mass, and because remote sensing techniques are affected by the thermal and haline gradients within the top millimeter of the ocean, the diffusive microlayer was also included in this scheme following the conceptual models and relations proposed by *Saunders* [1967] and *Schlussel et al*. [1997].

The scheme was used to simulate two rain-induced cooling events observed in the tropical Pacific Ocean: the rain-driven surface cooling events observed during the Palau2013 campaign and the rain event sampled during the Kilo Moana 2011 cruise [*Asher et al*., 2014b]. In the cooling event from the Palau2013 dataset, the surface cooling predicted by the prognostic model roughly captures the observed evolution of the surface temperature. In the second and weaker cooling event from Kilo Moana 2011, the scheme reproduces the decrease in salinity reasonably well but underestimates the temperature decrease. However, the scheme is able to reproduce the lifetime of the lens. Additionally, for the first cooling event with light wind conditions, the model also reproduces the lag of 2 h between the minimums in salinity and temperature. In the second case, characterized by higher wind speed on the average, there is no temporal lag between the minimums in temperature and salinity in either the observations or the simulations.

Additional calculations done using the model combined with detailed analysis of the observational data for these two cases suggest that the underestimation of the decrease in salinity or temperature may partly be due to the use of a constant value for η (see equation 11) for wind speeds below 2 m s^{-1}. In particular, with more field observations of fresh lenses it would become possible to parameterize η in terms of wind speed. However, a constant value of η for low wind speed was maintained because there are too few direct observations of rain-induced cooling events to develop such a parameterization. Furthermore, this parameterization for η leads to a good agreement between the salinity decreases calculated here and the salinity decreases that were parameterized in terms of U and R_{max} by *Drushka et al*. [2016] using numerical results from GOTM. Finally, the relationship between ΔS (or ΔT) calculated using the scheme and U and R shown in Figure 7 is comparable to drifter observations reported by *Reverdin et al*. [2012]. However, it should be noted that the wind-speed dependence of the idealized profiles proposed here is likely to be modified in the future after the analysis of further rain-induced lenses. In addition, the turbulence generated by the impact of raindrops on the ocean surface (τ_k) may be important in mixing of the first few centimeters of the ocean. Further observational and theoretical studies are, however, needed to take this effect into account for the sub-skin T and S.

The scheme accounts for the sensitivity of the decrease in S or T to the temporal distribution of rainfall. As reproduced by the scheme and discussed by *Drushka et al*. [2016], for a given total rain volume, the decrease in salinity or temperature is sensitive to the peak rain rate or, equivalently, to the duration of the rain event. The results presented here further suggest that the temperature decrease is a function of wind speed. When wind speed is low, the fresh lens has a longer lifetime, providing time for the surface heat fluxes to further cool the lens. Under these conditions, the temperature minimum occurs at some time after both the maximum rain rate and the salinity minimum. Furthermore, the decrease in surface temperature is larger when the duration of the rain event is longer (corresponding to a smaller peak rain intensity). This effect was observed in the Palau2013 dataset (Figure 1). In contrast, for strong winds, the decrease in salinity or temperature evolves in phase with each other and the rain forcing. Furthermore, the decrease in temperature is larger for shorter rain events with higher peak rain rates. Because the wind speed increases quickly during the second half of the rain event, the example from the KM11 experiment corresponds to this wind regime (Figure 3). This sensitivity to wind speed has implications on the diagnostic of rain-induced lenses using low temporal resolution datasets. Indeed, the lenses characteristics will then depend on the choice made for the interpolation of rainfall.

Finally, our scheme reproduces the sensitivity to solar radiation that was previously noted by *Reverdin et al*. [2012]. During daytime, the rain-induced cooling is offset by heating from solar radiation, which prevents destabilization of the lens. This is particularly effective in light wind conditions when the shortwave radiation heating is not transported downward by wind-induced turbulence.

In agreement with *Drushka et al*. [2016], the results presented here also suggest that surface cooling associated with rain-induced freshwater lenses can be on the same order of magnitude as the shortwave induced diurnal warming [e.g., *Stuart-Menteth et al*., 2003; *Gentemann et al*. 2003; *Bellenger and Duvel*, 2009; *Takaya et al*., 2010]. Additionally, both fresh lenses and diurnal warming have comparable lifetimes on order of several hours up to a day. It was shown that monthly means of the effects of rain-induced lenses on the western Pacific surface ocean state suggest that their impact is characterized by different temporal and spatial scales. The near surface temperature and salinity are more sensitive to precipitation distribution and are, therefore, a greater source of high frequency and small-scale variability. On the other hand, the microlayer effect is more closely linked to surface wind. In addition, in the case of temperature, the large diurnal warming also associated with weak wind conditions tend to offset the rain-induced lens effect on the average.

The complex interplay of these different effects on climate and its variability are still to be studied. We present here a tool to explore this impact at different temporal and spatial scales. The present scheme can indeed be employed in relatively high-resolution regional models and in climate and earth system models to assess the effect of fresh and cool lenses on the simulated climate and its variability in terms of SST and salinity and their impact on surface heat and chemical species fluxes (CO_2 for instance), oceanic mixed layer structure and atmospheric convection. *McCulloch et al*. [2012] discussed the potential impact of the absence of such rain-induced lens on surface flux and climate change projection by models. It seems, however, from the preliminary results presented here that their mean effect may be cancelled by the one of diurnal warm layers. Indeed, warm layers that are also light wind phenomena and are also absent from low-resolution climate models and should, therefore, be introduced together with the rain-induced lenses. Still a precise study of these counteracting phenomena, and their possible implication in various retroactions, has to be undertaken.

Acknowledgments
The Authors would like to thank J. Boutin, A. Ten Doeschate, K. Ando, and K. Yoneyama for interesting discussions. The authors also want to thank the editor and two anonymous reviewers for their help in improving significantly this manuscript. The Argo data (http://doi.org/10.17882/42182) are freely available by the International Argo Project and the national programs (http://www.argo.ucsd.edu, http://argo.jcommops.org). Argo is a pilot program of the Global Ocean Observing System. The gridded Argo data were produced by Dean Roemmich and John Gilson at Scripps Institution of Oceanography. NOAA provides CMORPH rainfall estimates. ECMWF provides ERA-Interim fields. The description of PALAU2013 campaign cruise description of the sensors that was deployed during this experiment can be found online: http://www.godac.jamstec.go.jp/catalog/doc_catalog/metadataDisp/MR13-03_leg1-2_all?lang=en. PALAU2013 data are available upon request to M. Katsumata (katsu@jamstec.go.jp). Requests concerning Kilo Moana 2011 cruise data should be directed to W. E. Asher (asherwe@apl.washington.edu). G. Reverdin acknowledges the support from CNES TOSCA SMOS project.

References

Asher, E. W., A. T. Jessup, and D. Clark (2014a), Stable near-surface ocean salinity stratifications due to evaporation observed during STRASSE, *J. Geophys. Res.*, *119*, 3219–3233, doi:10.1002/2014JC009808.

Asher, E. W., A. T. Jessup, R. Branch, and D. Clark (2014b), Observations of rain-induced near surface salinity anomalies, *J. Geophys. Res.*, *119*, 5483–5500, doi:10.1002/2014JC009954.

Bellenger, H., and J. P. Duvel (2009), An analysis of ocean diurnal warm layers over tropical oceans, *J. Clim.*, *22*, 3629–3646.

Bellenger, H., Y. N. Takayabu, T. Ushiyama, and K. Yoneyama (2010), Role of diurnal warm layers in the diurnal cycle of convection over the tropical Indian Ocean during MISMO, *Mon. Weather Rev.*, *138*, 2426–2433.

Best, A. (1950), The size distribution of raindrops, *Q. J. R. Meteorol. Soc.*, *76*, 16–36.

Boutin, J., N. Martin, G. Reverdin, X. Yin, and F. Gaillard (2013), Sea surface freshening inferred from SMOS and ARGO salinity: Impact of rain, *Ocean Sci.*, *9*, 183–192.

Boutin, J., N. Martin, G. Reverdin, S. Morisset, X. Lin, L. Centurioni, and N. Reul (2014), Sea surface salinity under rain cells: SMOS satellite and in situ drifters observations, *J. Geophys. Res.*, *119*, 5533–5545, doi:10.1002/2014JC010070.

Boutin, J., et al. (2016), Satellite and in situ salinity: Understanding near-surface stratification and sub-footprint variability, *Bull. Am. Meteorol. Soc.*, *97*, 1391–1407.

Burchard, H., K. Bolding, and M. R. Villarreal (1999), GOTM, a general ocean turbulence model: Theory, implementation and test cases, *Tech. Rep.*, 103 pp., EUR 18745 EN, European Commission, Luxembourg.

Caldwell, D. R., and W. P. Elliott (1971), Surface stresses produced by rainfall, *J. Phys. Oceanogr.*, *1*, 145–148.

Chiang, J. C. H., S. E. Zebiak, and M. A. Cane (2001), Roles of elevated heating and surface temperature gradients in driving anomalous surface winds over tropical oceans, *J. Atmos. Sci.*, *58*, 1371–1394.

Clark, N. E., L. Eber, R. M. Laurs, J. A. Renner, and J. F. T. Saur (1974), Heat exchange between ocean and atmosphere in the eastern north Pacific for 1961-71, NOAA *Tech. Rep.*, 108 p., NMFS SSRF-682, U.S. Dept. of Commerce, Washington, D. C.

Clayson, C. A., and D. Weitlich (2007), Variability of tropical diurnal sea surface temperature, *J. Clim.*, *20*, 334–352.

Craeye, C., and P. Schlussel (1998), Rainfall on the sea: Surface renewals and wave damping, *Boundary Layer Meteorol.*, *89*, 349–355.

Dee, D., et al. (2011), The ERA-Interim reanalysis: Configuration and performance of the data assimilation system, *Q. J. R. Meteorol. Soc.*, *137*, 553–597, doi:10.1002/qj.828.

DeMott, C. A., N. P. Klingaman, and S. J. Woolnough (2015), Atmosphere-ocean coupled processes in the Madden-Julian oscillation, *Rev. Geophys.*, *53*, 1099–1154, doi:10.1002/2014RG000478.

Donlon, C. J., and I. S. Robinson (1997), Observation of the oceanic thermal skin in the Atlantic ocean, *J. Geophys. Res.*, *102*, 18,585–18,606.

Donlon, C., et al. (2007), The global ocean data assimilation experiment high-resolution sea surface temperature pilot project, *Bull. Am. Meteorol. Soc.*, *88*, 1197–1213.

Drushka, K., S. T. Gille, and J. Sprintall (2014), The diurnal salinity cycle in the tropics, *J. Geophys. Res.*, *119*, 5874–5890, doi:10.1002/2014JC009924.

Drushka, K., W. E. Asher, B. Ward, and K. Walesby (2016), Understanding the formation and evolution of rain-formed fresh lenses at the ocean surface, *J. Geophys. Res.*, *121*, 2673–2689, doi:10.1002/2015JC011527.

Fairall, C. W., E. F. Bradley, J. Godfrey, G. Wick, J. B. Edson, and G. S. Young (1996), Cool-skin and warm-layer effects on sea surface temperature, *J. Geophys. Res.*, *101*, 1295–1308.

Fairall, C. W., A. B. White, J. B. Edson, and J. E. Hare (1997), Integrated shipboard measurements of the marine boundary layer, *J. Atmos. Oceanic Technol.*, *14*, 338–359.

Fairall, C. W., E. F. Bradley, J. E. Hare, A. A. Grachev, and J. B. Edson (2003), Bulk parameterization of air-sea fluxes: Updates and verification for the COARE algorithm, *J. Clim.*, *16*, 571–591.

Farrar, J. T., C. J. Zappa, R. A. Weller, and A. T. Jessup (2007), Sea surface temperature signatures of oceanic internal waves in low winds, *J. Geophys. Res.*, *112*, C06014, doi:10.1029/2006JC003947.

Fay, J. A. (1969), The spread of oil slicks on a calm sea, in *Oil on the Sea*, edited by D. P. Hoult, pp. 53–63, Plenum, Springer, US.

Gentemann, C. L., C. J. Donlon, A. Stuart-Menteth, and F. J. Wentz (2003), Diurnal signals in satellite sea surface temperature measurements, *Geophys. Res. Lett.*, *30*(3), 1140, doi:10.1029/2002GL016291.

Gordon, A. L., and C. F. Giulivi (2008), Sea surface salinity trends over fifty years within the subtropical North Atlantic, *Oceanography*, *21*, 20–29.

Gordon, A. L. (2016), The marine hydrological cycle: The ocean's floods and droughts, *Geophys. Res. Lett.*, *43*, 7649–7652.

Gosnell, R., C. W. Fairall, and P. J. Webster (1995), The sensible heat of rainfall in the tropical ocean, *J. Geophys. Res.*, *100*, 18,437–18,442.

Hamada, A., Y. Murayama, and Y. N. Takayabu (2014), Regional characteristics of extreme rainfall extracted from TRMM PR measurements, *J. Clim.*, *27*, 8151–8169.

Henocq, C., J. Boutin, G. Reverdin, F. Petitcolin, S. Arnaud, and P. Lattes (2010), Vertical variability of near-surface salinity in the tropics: Consequences for L-band radiometer calibration and validation, *J. Atmos. Oceanic Technol.*, *27*, 192–209.

Houghton, D. (1969), Acapulco'68, *Weather*, *24*, 2–18.

Huppert, H. E., and J. E. Simpson (1980), The slumping of gravity currents, *J. Fluid Mech.*, *99*(4), 785–799.

Jessup, A. T., and V. Hesany (1996), Modulation of ocean skin temperature by swell waves, *J. Geophys. Res.*, *101*, 6501–6511.

Joyce, R. J., J. E. Janowiak, P. A. Arkin, and P. Xie (2004), CMORPH: A method that produces global precipitation estimates from passive microwave and infrared data at high spatial and temporal resolution, *J. Hydrometeorol.*, *5*(3), 487–503.

Katsaros, K. B. (1976), Effects of precipitation on the eddy exchange in a wind driven sea, *Dyn. Atmos. Oceans*, *1*, 99–126.

Katsaros, K., and K. J. K. Buettner (1969), Influence of rainfall on temperature and salinity of the ocean surface, *J. Appl. Meteorol.*, *8*, 15–18.

Kawai, Y., H. Kawamura, S. Tanba, K. Ando, K. Yoneyama, and N. Nagahama (2006), Validity of sea surface temperature observed with the TRION buoy under diurnal heating conditions, *J. Oceanogr.*, *62*, 825–838.

Kudryavtsev, V. N., and A. V. Soloviev (1990), Slippery near-surface layer of the ocean arising due to daytime solar heating, *J. Phys. Oceanogr.*, *20*, 617–628.

Large, W. G., J. C. McWilliams, and S. C. Doney (1994), Oceanic vertical mixing: A review and a model with a nonlocal boundary layer parameterization, *Rev. Geophys.*, *32*, 363–403.

Li, Y., and R. E. Carbone (2012), Excitation of rainfall over the tropical western Pacific, *J. Atmos. Sci.*, *69*, 2983–2994.

Lindstrom, E., F. Bryan, and R. Schmitt (2015), SPURS: Salinity Processes in the Upper-ocean Regional Study—The North Atlantic Experiment, *Oceanography*, *28*(1), 14–19.

Manton, M. J. (1973). On the attenuation of sea waves by rain, *Geophys. Fluid Dyn.*, *5*, 249–260.

Marshall, J. S., and W. McK. Palmer (1948), The distribution of raindrops with size, *J. Meteorol.*, *5*, 165–166.

McCulloch, M. E., P. Spurgeon, and A. Chuprin (2012), Have mid-latitude ocean rain-lenses been seen by the SMOS satellite? *Ocean Modell.*, *43-44*, 108–111.

Miller, J. R. (1976), The salinity effect in a mixed layer ocean model, *J. Phys. Oceanogr.*, *6*, 29–35.

Noh, Y., G. Goh, and S. Raash (2010), Examination of the mixed layer deepening process during convection using LES, *J. Phys. Oceanogr.*, *40*, 2189–2195.

Oguz, H. N., and Prosperetti (1991), Numerical calculation of the underwater noise of rain, *J. Fluid Mech.*, *228*, 417–442.

Paulson, C. A., and G. S. E. Lagerloef (1993), Fresh surface lenses caused by heavy rain over the western Pacific warm pool during TOGA COARE, *Eos Trans. AGU*, *74*(Suppl. To No. 43), 125.

Price, J. F. (1979), Observations of rain-formed mixed layer, *J. Phys. Oceanogr.*, *9*, 643–649.

Price, J. F., R. A. Weller, and R. Pinkel (1986), Diurnal cycling: Observations and models of the upper ocean response to diurnal heating, cooling, and wind mixing, *J. Geophys. Res.*, *91*, 8411–8427.

Reed, R. K. (1977) Om estimating insolation over the ocean, *J. Phys. Oceanogr.*, *7*, 482–485.

Reverdin, G., S. Morisset, J. Boutin, and N. Martin (2012), Rain-induced variability of near sea-surface T and S from drifter data, *J. Geophys. Res.*, *117*, C02032, doi:10.1029/2011JC007549.

Reverdin, G., S. Morisset, H. Bellenger, J. Boutin, N. Martin, P. Blouch, J. Rolland, F. Gaillard, P. Bouruet-Aubertot, and B. Ward (2013), Near-sea surface temperature stratification from SVP drifters, *J. Atmos. Oceanic. Technol.*, *30*, 1867–1883.

Ruppert, J. H., and R. H. Johnson (2015), Diurnally modulated cumulus moistening in the preonset stage of the Madden–Julian oscillation during DYNAMO*, *J. Atmos. Sci.*, *72*(4), 1622–1647.

Ruppert, J. H., Jr., and R. H. Johnson (2016), On the cumulus diurnal cycle over the tropical warm pool, *J. Adv. Model. Earth Syst.*, *8*, 669–690, doi:10.1002/2015MS000610.

Santos-Garcia, A., M. M. Jacob, W. L. Jones, W. E. Asher, Y. Hejazin, H. Ebrahimi, and M. Rabolli (2014), Investigation of rain effects on Aquarius sea surface salinity measurements, *J. Geophys. Res.*, *119*, 7605–7624, doi:10.1002/2014JC010137.

Saunders, P. M. (1967), The temperature at the ocean–air interface, *J. Atmos. Sci.*, *24*, 269–273.

Schlussel, P., A. V. Soloviev, and W. J. Emery (1997), Cool and freshwater skin of the ocean during rainfall, *Boundary Layer Meteorol.*, *82*, 437–472.

Schmitt, R. W. (2008), Salinity and the global water cycle, *Oceanography*, *21*, 12–19.

Soloviev, A., and R. Lukas (2006), *The Near-Surface Layer of the Ocean: Structure, Dynamics and Applications*, 572 pp, Springer, Dordrecht, Netherlands.

Soloviev A., S. Matt, and A. Fujimura (2015), Three-dimensional dynamics of fresh water lenses in the ocean's near surface layer, *Oceanography*, *28*(1), 142–149.

Stuart-Menteth, A. C., I. S. Robinson, and P. G. Challenor (2003), A global study of diurnal warming using satellite-derived sea surface temperature, *J. Geophys. Res.*, *108*(C5), 3155, doi:10.1029/2002JC001534.

Sui, C.-H., K.-M. Lau, Y. N. Takayabu, and D. A. Short (1997), Diurnal variations in tropical oceanic cumulus convection during TOGA COARE, *J. Atmos. Sci.*, *54*(1990), 639–655.

Sutherland, G., L. Marié, G. Reverdin, K. H. Christensen, G. Brostrom, and B. Ward (2016), Enhanced turbulence associated with the diurnal jet in the ocean surface boundary layer, *J. Phys. Oceanogr.*, *46*, 3051–3067.

Takaya, Y., J.-R. Bidlot, A. C. M. Beljaars, and P. A. E. M. Janssen (2010), Refinements to a prognostic scheme of skin sea surface temperature, *J. Geophys. Res.*, *115*, C06009, doi:10.1029/2009JC005985.

Tsimplis, M., and S. A. Thorpe (1989), Wave damping by rain, *Nature*, *342*, 893–895.

Ward, B., R. Wanninkhof, W. R. McGillis, A. T. Jessup, M. D. DeGrandpre, J. E. Hare, and J. B. Edson (2004), Biases in the air-sea flux of CO2 resulting from ocean surface temperature gradients, *J. Geophys. Res.*, *109*, C08S08, doi:10.1029/2003JC001800.

Wick, G. A., and A. T. Jessup (1998), Simulation of ocean skin temperature modulation by swell waves, *J. Geophys. Res.*, *103*, 3149–3161.

Webster, P. J., C. A. Clayson, and J. A. Curry (1996), Clouds, radiation, and the diurnal cycle of sea surface temperature in the tropical western Pacific, *J. Clim.*, *9*, 1712–1730.

Woods, J. D., and V. Strass (1986), The response of the upper ocean to solar heating. II: The wind-driven current, *Q. J. R. Meteorol. Soc.*, *112*, 29–42.

Zeng, X., and A. Beljaars (2005), A prognostic scheme of sea surface skin temperature for modeling and data assimilation, *Geophys. Res. Lett.*, *32*, L14605, doi:10.1029/2005GL023030.

Erratum

In the originally published version of this article, the was a typographical error in the equation in the first line on on page 5. This has since been corrected, and this version may be considered the authoritative version of record.

In the originally published version of this paper, there was an error in the values for Equation 8. The correct values are: $a = 4 \times 10^{-4}$ and $b = 1.3$. These corrections have since been made to the online version only, which may be considered the authoritative version.